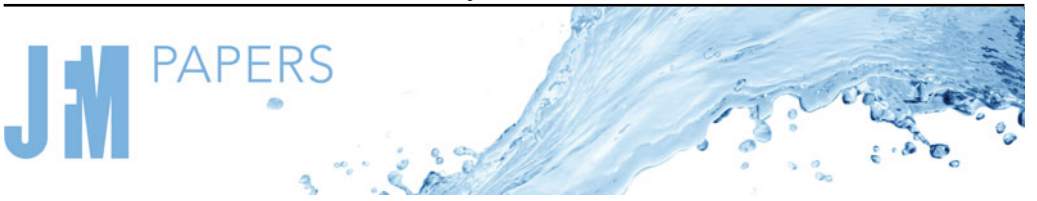
J. Fluid Mech. (2026), *vol.* 1040, A26, doi:10.1017/jfm.2026.11872



Bidirectional shallow-water wave turbulence

Ashleigh Simonis[1], **Sergey Nazarenko**[2], **Jalal Shatah**[3] **and Yulin Pan**[1]

[1]Department of Naval Architecture and Marine Engineering, University of Michigan, 2600 Draper Drive, Ann Arbor, MI 48109, USA

[2]Institut de Physique de Nice, Université Côte d'Azur et CNRS, 17 rue Julien Lauprêtre, 06200 Nice, France

[3]Courant Institute of Mathematical Sciences, New York University, 251 Mercer Street, New York, NY 10012, USA

Corresponding authors: Ashleigh Simonis, asimonis@umich.edu; Yulin Pan, yulinpan@umich.edu

(Received 31 March 2026 UTC; revised 24 June 2026 UTC; accepted 26 June 2026 UTC)

We study bidirectional one-dimensional (1-D) shallow-water waves within a class of Boussinesq equations, including the integrable Kaup–Boussinesq (KB) equation and a truncated-dispersion variant, which serves as a representative non-integrable model. For these two systems, the normal-form transformation yields an interaction coefficient of the same general structure, differing only through the dispersion relation. We derive this coefficient and numerically confirm that it vanishes on the resonant manifold for the KB equation, as expected from integrability. In contrast, the non-integrable model admits a non-vanishing interaction coefficient consistent with broken integrability, producing a non-trivial wave kinetic equation (WKE), which is the first known in a 1-D shallow-water setting. The resulting WKE is non-homogeneous in nature due to the non-homogeneity of the corresponding dispersion relation; however, approximate Kolmogorov–Zakharov solutions can be derived in a novel way under certain approximations. Numerical experiments in two settings validate the kinetic predictions and elucidate the underlying dynamics: (i) in free-evolution cases of the KB equation, despite complete integrability and the invariance of the discrete nonlinear spectrum guaranteed by isospectrality, an initial arbitrary wavenumber spectrum undergoes substantial evolution driven by quasi-resonant triad interactions and (ii) in forced-dissipated cases of the non-integrable equation, we find stationary power-law spectra that agree with the theoretical predictions.

Key words: turbulence theory

© The Author(s), 2026. Published by Cambridge University Press. This is an Open Access article, distributed under the terms of the Creative Commons Attribution licence (https://creativecommons.org/licenses/by/4.0/), which permits unrestricted re-use, distribution and reproduction, provided the original article is properly cited.

https://doi.org/10.1017/jfm.2026.11872 Published online by Cambridge University Press

1. Introduction

Wave kinetic theory describes the long-time statistical evolution of weakly nonlinear dispersive waves, predicting irreversible spectral transfer towards either a thermal equilibrium state or a Kolmogorov–Zakharov (KZ) cascade (e.g. Nazarenko 2011; Zakharov *et al.* 2012). While this theory is well developed for deep-water waves, beginning with Hasselmann's derivation of the wave kinetic equation (WKE) (Hasselmann 1962), its shallow-water counterpart is less understood in the literature. For two-dimensional (2-D) shallow-water surface waves, the theory has been studied starting from either the Euler equations (Zakharov 1999) or the Boussinesq equations (Onorato *et al.* 2009), with their predictions of the KZ spectrum observed in wave tank experiments (Kaihatu *et al.* 2007) and in detailed numerical studies (Clark di Leoni *et al.* 2014). However, in the one-dimensional (1-D) setting, there is currently no established theory for wave turbulence, as many contend the dynamics can be described by integrable models (Zakharov *et al.* 2012), such as the Korteweg–de Vries (KdV), Kadomtsev–Petviashvili-2, Camassa–Holm and Kaup–Boussinesq (KB) equations. This line of reasoning is due in part to the widely held empirical belief that integrable systems do not admit non-trivial kinetic descriptions (e.g. Zakharov & Schulman 1980, 1988; Zakharov 1991).

The purpose of this paper is to revisit the largely underexplored problem of wave turbulence in bidirectional 1-D shallow-water waves, starting from the *abcd* class of Boussinesq equations, which provide descriptions of the dynamics in the long-wave regime. This class includes the completely integrable KB equation (e.g. Kaup 1975; Kupershmidt 1985; El *et al.* 2001; Ivanov 2009; Bhrawy *et al.* 2013; Gong & Wang 2022; Klein & Saut 2025), as well as several well-known non-integrable models such as the classical Boussinesq, Bona–Smith and Benjamin–Bona–Mahony systems (e.g. Bona, Chen & Saut 2002, 2004). From an experimental perspective, studies of bidirectional shallow-water waves (e.g. Redor *et al.* 2019, 2021; Leduque *et al.* 2025) have demonstrated a range of behaviours, including spectral evolution towards a flat energy spectrum at large scales (interpreted as Rayleigh–Jeans (RJ) distribution in Pelinovsky & Sergeeva (Kokorina) (2006)) and/or the emergence of a soliton gas, depending on the system nonlinearity and forcing condition. These observations suggest that it is problematic to view either the completely integrable KB equation or standard non-integrable Boussinesq equations as a standalone, canonical model for 1-D bidirectional shallow-water waves, as each only accounts for a subset of the results, i.e. integrable features in the former and more traditional wave kinetic behaviour in the latter.

To develop a comprehensive understanding of both integrable and non-integrable dynamics, we consider the completely integrable KB equation and a truncated-dispersion variant representing the non-integrable setting. Although exact dispersion relations differ across the *abcd* class, this truncation retains the common leading-order long-wave dispersive behaviour. A normal-form transformation can be applied to the models considered to remove the quadratic terms, for which we carefully characterise its validity condition depending on the parameters α and β measuring the nonlinearity and dispersion. This yields an interaction coefficient of the same general form for both cases, differing only in the dispersion relation. For the KB equation, we numerically confirm that the interaction coefficient is zero exactly on the four-wave resonant manifold, consistent with the prevailing view in the literature (e.g. Zakharov & Schulman 1980, 1988; Zakharov 1991). In contrast, when considering the truncated-dispersion model, our analysis yields a non-zero interaction coefficient that can be reduced to a compact form, clearly demonstrating non-trivial wave kinetics. The resulting WKE is inherently non-homogeneous due to the

https://doi.org/10.1017/jfm.2026.11872 Published online by Cambridge University Press

inhomogeneity of the dispersion relation. While the thermal equilibrium spectra remain as exact stationary solutions, the KZ solutions must be derived under approximations in a novel way. We derive two distinct direct cascade solutions corresponding to the limits of small and large modal amplitudes at low wavenumbers, given respectively by $n_k \sim |k|^{-3}$ and $n_k \sim |k|^{-3/2}$, with each corresponding to a local solution of the WKE.

We proceed to perform direct numerical simulations, both to test the validity of our theoretical predictions and to investigate the underlying mechanism of energy transfer. We start by demonstrating a free-evolution case of the KB equation from random-wave initial conditions, where the discrete eigenvalues obtained from the direct scattering transform (representing solitons present in the initial field) remain constant in time, while the wavenumber spectrum quickly evolves towards a state consistent with the RJ scaling. This case demonstrates that, despite the KB equation being completely integrable and maintaining isospectrality of the eigenvalues, it can still exhibit significant spectral evolution due to quasi-resonant triad interactions. We then turn to simulations of the forced-dissipated non-integrable Boussinesq equation, where the low-wavenumber modal amplitude is controlled through the presence of the low-wavenumber dissipation. For small and large modal amplitudes at low wavenumbers, respectively, we reproduce the two theoretical KZ solutions. We also discuss how wave kinetic behaviour may become possible even in the full KB model as a result of four-wave quasi-resonant interactions. This is due to the previously unidentified near-singular behaviour of the interaction coefficient near the resonant manifold. A more detailed study is left for future work.

We finally remark that the wave kinetic behaviour we discover in the present paper is fundamentally different from Janssen's WKE for the 1-D nonlinear Schrödinger equation (Janssen 2003), as well as the notion of 'integrable turbulence' (e.g. Agafontsev & Zakharov 2015, 2016; Randoux *et al.* 2016; Roberti *et al.* 2019; El 2021; Bonnemain *et al.* 2022; Suret *et al.* 2024). The former describes a time-dependent collision integral that vanishes as $t \to \infty$ (thus saturating to a steady-state spectrum), whereas the latter may refer to a soliton-gas state in an integrable model, described statistically by a kinetic theory for the ensemble of solitons. It is often assumed that the soliton-gas state is the only physically relevant phenomenon for 1-D shallow-water waves. Our results demonstrate that this is not the case, as free-wave, non-resonant interactions and spectral transfer may occur in a more traditional wave-turbulence sense, providing insight into integrable systems in a broader context. Taken together with the non-integrable Boussinesq case, which supports true resonant interactions and a non-trivial WKE, these results establish a robust theoretical framework for 1-D shallow-water wave turbulence.

2. Theoretical derivation

2.1. *Derivation of the wave kinetic equation*

In this section, we use the KB equation as a starting point to develop a generalised framework that we apply to two representative cases within the *abcd* class of Boussinesq equations. The resulting normal-form interaction coefficient has the same general structure in these cases, with the dispersion relation being the only model-dependent component. We examine the interaction coefficient for both the full KB variant and its truncated-dispersion version.

The dimensional KB system is given by

$$\eta_t + [(h+\eta)u]_x = -\frac{h^3}{3}u_{xxx}, \tag{2.1}$$

https://doi.org/10.1017/jfm.2026.11872 Published online by Cambridge University Press

$$u_t + uu_x + g\eta_x = 0, \tag{2.2}$$

where $\eta(x,t)$ denotes the surface elevation, $u(x,t)$ is the fluid velocity, g is the acceleration of gravity and h is the water depth. The system of (2.1) and (2.2) is known to be completely integrable in the inverse scattering method sense (Kaup 1975). We introduce the following non-dimensional variables:

$$\tilde{\eta} = \eta/a, \quad \tilde{x} = x/L_p, \quad \tilde{t} = t/(L_p/\sqrt{gh}), \quad \tilde{u} = u/\left(\sqrt{gh}\frac{a}{h}\right). \tag{2.3}$$

where a denotes the characteristic wave amplitude (e.g. half the significant wave height H_s) and L_p is the peak wavelength of the wave field. Substituting (2.3) into (2.1) and (2.2) and omitting the tilde notation, we obtain

$$\eta_t + u_x + \alpha(\eta u)_x = -\frac{1}{3}\beta u_{xxx}, \tag{2.4}$$

$$u_t + \eta_x + \alpha u u_x = 0, \tag{2.5}$$

where $\alpha = a/h$ and $\beta = (h/L_p)^2$ are dimensionless measures of nonlinearity and dispersion, respectively.

We consider (2.4) and (2.5) on a periodic domain $\mathbb{T}_L$. Defining Fourier-domain variables such as $\hat{\eta}_k(t) = \int_0^L \eta(x,t)\mathrm{e}^{-ikx}\,\mathrm{d}x/L$ (note that k can be positive or negative), (2.4) and (2.5) can be transformed into

$$\frac{\partial \hat{\eta}_k}{\partial t} + i\left(k - \frac{1}{3}\beta k^3\right)\hat{u}_k + i\alpha \sum_{k_1+k_2=k} k\hat{\eta}_{k_1}\hat{u}_{k_2} = 0, \tag{2.6}$$

$$\frac{\partial \hat{u}_k}{\partial t} + ik\hat{\eta}_k + \frac{i}{2}\alpha \sum_{k_1+k_2=k} k\hat{u}_{k_1}\hat{u}_{k_2} = 0. \tag{2.7}$$

The linear part of (2.6) and (2.7) yields the dispersion relation

$$\omega_k = \kappa\sqrt{1 - \frac{1}{3}\beta\kappa^2}, \tag{2.8}$$

where $\kappa = |k|$. Assuming $\beta\kappa^2 \ll 1$, we expand in the small parameter $\beta\kappa^2$ and retain terms through first order:

$$\omega_k = \kappa\left(1 - \frac{\beta}{6}\kappa^2\right). \tag{2.9}$$

This approximation defines the truncated-dispersion variant of (2.6) and (2.7), whereas the same equations with the full dispersion relation (2.8) are referred to as the full KB equation. This truncated form captures the leading-order dispersive behaviour of non-integrable models in the *abcd* class (e.g. Bona *et al.* 2002, 2004). Both (2.8) and (2.9) agree with the shallow-water dispersion relation $\omega_k = \kappa$ when $\beta\kappa^2 \ll 1$, but depart significantly from it on the descending branch:

$$\kappa > \kappa_*, \qquad \left.\frac{\mathrm{d}\omega}{\mathrm{d}\kappa}\right|_{\kappa=\kappa_*} = 0, \tag{2.10}$$

where $\kappa_* = \sqrt{3/(2\beta)}$ for the full KB equation and $\kappa_* = \sqrt{2/\beta}$ for the truncated variant. In practice, we limit to a finite wavenumber range $\kappa_{max} < \kappa_*$, omitting the descending branch to ensure we remain in the near-shallow-water regime for the subsequent theoretical and numerical analyses.

https://doi.org/10.1017/jfm.2026.11872 Published online by Cambridge University Press

By defining the canonical variables

$$\hat{\eta}_k = \frac{\sqrt{2}}{2}\omega_k^{1/2}\left(a_k + a_{-k}^*\right) \tag{2.11}$$

and

$$\hat{u}_k = \frac{\sqrt{2}}{2}\frac{k}{\omega_k^{1/2}}\left(a_k - a_{-k}^*\right), \tag{2.12}$$

leading to

$$a_k = \frac{\sqrt{2}}{2}\omega_k^{-1/2}\hat{\eta}_k + \frac{\sqrt{2}}{2}\frac{\omega_k^{1/2}}{k}\hat{u}_k, \tag{2.13}$$

we can diagonalise (2.6) and (2.7) in the variable a_k:

$$\frac{\partial a_k}{\partial t} + i\omega_k a_k + \frac{i\alpha}{4\sqrt{2}}\sum_{k_1+k_2=k}\left\{U_{k12}a_{k_1}a_{k_2} - U_{k12}a_{k_1}a_{-k_2}^* + S_{k12}a_{-k_1}^*a_{k_2} - S_{k12}a_{-k_1}^*a_{-k_2}^*\right\} = 0, \tag{2.14}$$

where

$$U_{k12} = [2W(k,2) + W(1,2)](\omega_k\omega_{k_1}\omega_{k_2})^{1/2}, \tag{2.15}$$

$$S_{k12} = [2W(k,2) - W(1,2)](\omega_k\omega_{k_1}\omega_{k_2})^{1/2}, \tag{2.16}$$

with

$$W(k,j) = \frac{kk_j}{\omega_k\omega_{k_j}}, \qquad W(i,j) = \frac{k_ik_j}{\omega_{k_i}\omega_{k_j}}. \tag{2.17}$$

Manipulating (2.14) using symmetry conditions, we get the final canonical equation:

$$\frac{\partial a_k}{\partial t} + i\omega_k a_k + i\left\{\sum_{k_1+k_2=k}V_{k12}a_{k_1}a_{k_2} + \sum_{k_1-k_2=k}V_{k12}a_{k_1}a_{k_2}^* + \sum_{k_2-k_1=k}V_{k12}a_{k_1}^*a_{k_2} + \sum_{k_2+k_1+k=0}V_{k12}a_{k_1}^*a_{k_2}^*\right\} = 0, \tag{2.18}$$

where

$$V_{k12} = \frac{\alpha(\omega_k\omega_{k_1}\omega_{k_2})^{1/2}}{4\sqrt{2}}[W(k,1) + W(k,2) + W(1,2)]. \tag{2.19}$$

We note that all interaction kernels in (2.18) are the same, which is consistent with the case in the 2-D Boussinesq equation derived in Onorato *et al.* (2009).

Our next goal is to apply a normal-form transformation (or multiple time scale method) to (2.18) with the aim of eliminating the quadratic nonlinear terms, since the dispersion relation (2.8) does not support triad resonant interactions. This approach has been previously applied to the 2-D Euler equations for shallow water (Zakharov 1999) and to the 2-D Boussinesq equations (Onorato *et al.* 2009). The procedure is standard (e.g. Krasitskii 1994; Zakharov *et al.* 2012) except for the validity condition of the transformation, which is discussed later.

https://doi.org/10.1017/jfm.2026.11872 Published online by Cambridge University Press

We proceed by applying the normal-form transformation method to introduce a new variable b_k defined as

$$\begin{aligned} a_k = b_k &+ \sum_{k_1+k_2=k} \Gamma^{[1]}_{k12} b_{k_1} b_{k_2} - 2 \sum_{k_2-k_1=k} \Gamma^{[1]}_{2k1} b^*_{k_1} b_{k_2} + \sum_{k_1+k_2+k=0} \Gamma^{[2]}_{k12} b^*_{k_1} b^*_{k_2} \\ &+ \sum_{k+k_1=k_2+k_3} B_{k123} b^*_{k_1} b_{k_2} b_{k_3} + \text{other cubic terms}, \end{aligned} \tag{2.20}$$

such that, rewriting (2.18) in terms of b_k and retaining terms up to cubic order, yields

$$\frac{\partial b_k}{\partial t} + i\omega_k b_k + i \sum_{k+k_1=k_2+k_3} T_{k123} b^*_{k_1} b_{k_2} b_{k_3} = 0. \tag{2.21}$$

This transformation is achieved by appropriately choosing the coefficients in (2.20), for example,

$$\Gamma^{[1]}_{k12} = \frac{-V_{k12}}{\omega_k - \omega_1 - \omega_2}, \quad \Gamma^{[2]}_{k12} = \frac{-V_{k12}}{\omega_k + \omega_1 + \omega_2}. \tag{2.22}$$

The interaction kernel in (2.21) is given by

$$\begin{aligned} T_{k123} = &- V_{k,2,k-2} V_{3,1,3-1} \left[\frac{1}{\omega_2 + \omega_{k-2} - \omega_k} + \frac{1}{\omega_1 + \omega_{3-1} - \omega_3} \right] \\ &- V_{1,2,1-2} V_{3,k,3-k} \left[\frac{1}{\omega_2 + \omega_{1-2} - \omega_1} + \frac{1}{\omega_k + \omega_{3-k} - \omega_3} \right] \\ &- V_{k,3,k-3} V_{2,1,2-1} \left[\frac{1}{\omega_3 + \omega_{k-3} - \omega_k} + \frac{1}{\omega_1 + \omega_{2-1} - \omega_2} \right] \\ &- V_{1,3,1-3} V_{2,k,2-k} \left[\frac{1}{\omega_3 + \omega_{1-3} - \omega_1} + \frac{1}{\omega_k + \omega_{2-k} - \omega_2} \right] \\ &- V_{k+1,k,1} V_{2+3,2,3} \left[\frac{1}{\omega_{k+1} - \omega_k - \omega_1} + \frac{1}{\omega_{2+3} - \omega_2 - \omega_3} \right] \\ &- V_{-k-1,k,1} V_{-2-3,2,3} \left[\frac{1}{\omega_{k+1} + \omega_k + \omega_1} + \frac{1}{\omega_{2+3} + \omega_2 + \omega_3} \right]. \end{aligned} \tag{2.23}$$

We observe that T_{k123} in (2.23) possesses the desired symmetry properties, namely $T_{k123} = T_{1k23} = T_{k132} = T_{23k1}$.

To obtain the above results, the transformation $a_k \to b_k$ defined in (2.20) must be near-identity. As discussed in Zakharov (1999), this requires

$$\left| \sum_{k_1+k_2=k} \Gamma^{[1]}_{k12} b_{k_1} b_{k_2} - 2 \sum_{k_2-k_1=k} \Gamma^{[1]}_{2k1} b^*_{k_1} b_{k_2} + \sum_{k_1+k_2+k=0} \Gamma^{[2]}_{k12} b^*_{k_1} b^*_{k_2} \right| \ll |b_k|. \tag{2.24}$$

In formulating (2.24), inconsistencies arise in Zakharov (1999). In particular, the analysis in Zakharov (1999) does not account for the random phases of b_k when estimating the summations on the left-hand side, resulting in an overestimation. In Appendix A, we provide a new estimation that properly incorporates phase randomness to derive the validity condition for the normal-form transformation (see also Wu *et al.* 2025). The result is straightforward and can be summarised as follows:

We consider a spectrum with finite bandwidth Δ in k, assuming that it decays sufficiently fast outside Δ. Then (2.24) *corresponds to the condition of* $\alpha \ll \beta$. While the detailed

https://doi.org/10.1017/jfm.2026.11872 Published online by Cambridge University Press

derivation is provided in Appendix A, the underlying logic is to avoid small denominators arising on the left-hand side of (2.24). The most singular term in the denominator is of $O(\beta)$, which must be significantly larger than the numerator of $O(\alpha)$.

Starting from (2.21), we formally derive the corresponding WKE following standard procedures (e.g. Nazarenko 2011). The WKE is given by

$$\frac{\partial n_k}{\partial t} = 4\pi \int |T_{k123}|^2 n_k n_1 n_2 n_3 \left[\frac{1}{n_k} + \frac{1}{n_1} - \frac{1}{n_2} - \frac{1}{n_3}\right] \times \delta(k + k_1 - k_2 - k_3)\delta(\omega_k + \omega_1 - \omega_2 - \omega_3)\,\mathrm{d}k_1\,\mathrm{d}k_2\,\mathrm{d}k_3, \tag{2.25}$$

where $n_k = \langle b_k b_k^* \rangle$ denotes the wave action, with $\langle a_k a_k^* \rangle = \langle b_k b_k^* \rangle + O(\alpha^2)$.

To determine whether (2.25) is trivial or not, it is essential to analyse the interaction coefficient T_{k123} on the resonant manifold defined by the resonance condition in (2.25). We begin by emphasising that for any concave-down dispersion relation, such as (2.8) and (2.9), the resonance condition in frequency ω cannot be satisfied if all wavenumbers involved share the same sign (i.e. all positive or all negative). Non-trivial resonant interactions occur only when one wavenumber has the opposite sign to the other three (e.g. one negative and three positive), or when two wavenumbers are positive and two are negative. The two-positive-two-negative configuration, however, requires at least one large wavenumber on the descending branch (2.10). Since both models have deviated substantially from the true shallow-water dispersion in this range, these interactions lie outside the regime of interest (i.e. $\kappa > \kappa_{max}$), and are therefore regarded as spurious solutions that may be discarded. A graphical proof of the resonance configurations, exemplified using (2.9), is provided in Appendix B, and is fundamental to the subsequent analysis of T_{k123}.

We begin our analysis with the KB equation with the dispersion relation (2.8). According to the literature (e.g. Zakharov & Schulman 1980, 1988; Zakharov 1991), we expect this system to yield a trivial interaction coefficient on the resonant manifold due to its complete integrability. Proving the coefficient vanishes on the resonant manifold for (2.8) is non-trivial, as the manifold lacks a simple analytical expression due to the square root. The next best approach is to verify numerically whether (2.23) vanishes on the resonant manifold. To this end, we compute T_{k123} for a large number of resonant quartets using the dispersion relation (2.8), with all computations carried out using quadruple precision. Table 1 presents a subset of these quartets tracing the resonant manifold, demonstrating that the resulting coefficient vanishes to numerical precision, which implies that the KB equation yields a trivial WKE.

Next, we move on to the analytical calculation for the non-integrable Boussinesq variant with dispersion relation (2.9). The existing view for the shallow-water wave interaction coefficient, such as (2.23), is that it contains both near-singular and regular terms (Zakharov 1999; Onorato *et al.* 2009). The former correspond to frequency mismatches of $O(\beta)$ (i.e. their inverses are of $O(1/\beta)$, which is near-singular), while the latter are of $O(1)$. It has previously been thought that the near-singular terms dominate the coefficient T_{k123}. However, the near-singular versus regular terms need to be evaluated through a much more delicate analysis, which we perform below.

Without loss of generality, we consider k, k_1, k_2 to be positive and k_3 to be negative, such that $\kappa_2 > \kappa, \kappa_1, \kappa_3$. Under this assumption, the 'near-singular' and 'regular' terms in (2.23) (hereafter named as T_I and T_{II}) can be collected as

https://doi.org/10.1017/jfm.2026.11872 Published online by Cambridge University Press

k	k_1	k_2	k_3	$\lvert T_{k123}\rvert$
5.0	1.982387	7.0	-1.76×10^{-2}	4.66×10^{-32}
5.0	2.969726	8.0	-3.03×10^{-2}	4.47×10^{-31}
5.0	3.954433	9.0	-4.56×10^{-2}	6.76×10^{-31}
5.0	4.936444	10.0	-6.36×10^{-2}	3.50×10^{-31}
5.0	5.915683	11.0	-8.43×10^{-2}	4.36×10^{-31}
5.0	6.892058	12.0	-1.08×10^{-1}	7.05×10^{-31}
5.0	7.865463	13.0	-1.35×10^{-1}	2.63×10^{-31}
5.0	8.835773	14.0	-1.64×10^{-1}	4.30×10^{-31}
5.0	9.802847	15.0	-1.97×10^{-1}	1.58×10^{-31}
5.0	10.766521	16.0	-2.33×10^{-1}	1.86×10^{-31}

Table 1. Values of the interaction coefficient T_{k123} for the KB equation using $\beta = 0.001$ for different resonant quartets.

$$T_I = -\frac{V_{k,3,k-3}V_{2,1,2-1}}{\omega_1+\omega_{2-1}-\omega_2} - \frac{V_{1,3,1-3}V_{2,k,2-k}}{\omega_k+\omega_{2-k}-\omega_2} - \frac{V_{k+1,k,1}V_{2+3,2,3}}{\omega_{k+1}-\omega_k-\omega_1}, \tag{2.26a}$$

$$T_{II} = T_{k123} - T_I. \tag{2.26b}$$

Substitution of (2.9) and (2.19) into (2.26) gives (see details in Appendix C)

$$T_I = -\frac{3\alpha^2}{16\beta}\left(\frac{\kappa_3^3}{\kappa\kappa_1\kappa_2}\right)^{1/2}, \tag{2.27a}$$

$$T_{II} = -\frac{\alpha^2}{64}(\kappa\kappa_1\kappa_2\kappa_3)^{1/2}\left[\kappa_3\left(\frac{1}{\kappa_1}-\frac{1}{\kappa_2}+\frac{1}{\kappa}\right)\right]. \tag{2.27b}$$

At first glance, the relative magnitude of these two contributions in the small-β limit is not immediately clear from (2.27*a*,*b*). However, solving the resonance condition in (2.25) gives $\kappa_3 = (\beta/4)\kappa\kappa_1\kappa_2$ (see Appendix D); substituting this into (2.27*a*,*b*) yields

$$T_I = -\frac{3\alpha^2}{128}\beta^{1/2}\kappa\kappa_1\kappa_2, \tag{2.28a}$$

$$T_{II} = -\frac{\alpha^2}{512}\beta^{3/2}\kappa\kappa_1\kappa_2(\kappa\kappa_2+\kappa_1\kappa_2-\kappa\kappa_1). \tag{2.28b}$$

Thus, for small β, the T_I dominates, and the total coefficient can be reduced to the compact leading-order form

$$T_{k123} \approx T_I = -\frac{3\alpha^2}{128}\beta^{1/2}\kappa\kappa_1\kappa_2. \tag{2.29}$$

We note that if any wavenumber other than k_3 is chosen to be negative (with the others positive), the coefficient T_{k123} can be directly evaluated using its symmetry properties. For example, if $k_1 < 0$, one can use the relation $T_{k123} = T_{231k}$, where the latter evaluates to $T_{231k} = -(3\alpha^2/128)[\sqrt{\beta}\kappa\kappa_2\kappa_3]$. Consequently, a general expression for T_{k123} can be written as

$$T_{k123} = -\frac{3\alpha^2}{128}\left(\sqrt{\beta}\kappa_{mul}\right), \tag{2.30}$$

https://doi.org/10.1017/jfm.2026.11872 Published online by Cambridge University Press

where κ_{mul} represents the multiplication of the magnitudes of the three wavenumbers with the same sign.

We also remark here that it is claimed in Zakharov (1999) that all 'near-singular' terms in T_{k123} cancel out, based on the formulation from the Euler equation. This claim is in fact not relevant to the present case, since Zakharov (1999) assumes that all wavenumbers share the same sign, which is not consistent with the resonant manifold in (2.25).

Since $T_{k123} \neq 0$ on the resonant manifold according to (2.30), we have obtained a non-trivial WKE (2.25) from (2.4) and (2.5) with a truncated-dispersion relation approximation. Next, we seek stationary solutions to (2.25). The first set of stationary solutions is of RJ type, namely the equipartition-of-action solution $n_k \sim \kappa^0$ and the equipartition-of-energy solution $n_k \sim 1/\omega_k \cong 1/\kappa^1$. These naturally hold for (2.25) since they turn the integrand in the integral on the right-hand side into zero at each point. However, the KZ turbulent solution to (2.25) needs to be found in a novel way, which we describe in the following section.

2.2. *Kolmogorov–Zakharov spectra*

One might attempt to find the KZ solution $n_k \sim \kappa^\gamma$ to (2.25) using a 'standard' approach using the formula $\gamma = -2\tau/3 - 1$ (Nazarenko 2011) with τ the degree of homogeneity of T_{k123}. However, this approach does not hold here because the dispersion relation (2.9) is inhomogeneous, which breaks the basis to derive the 'standard' formula. As one may have noticed here, even the degree of homogeneity τ is not certain here, depending on whether (2.27*a*,*b*) or (2.28) is used for evaluation, which results from the same inhomogeneity issue. If one simply considers a dispersion relation $\omega_k = \kappa$ with $\beta = 0$, then the resonance condition leads to $\kappa_3 = 0$ in (2.27*a*,*b*) so that $T_{k123} = 0$ and the problem becomes trivial. Therefore, to obtain the KZ spectrum, we have to develop a refined approach which considers the cubic terms in the dispersion relation (as we have done in deriving (2.28)).

We start by considering an isotropic spectrum, $n_{-k} = n_k$, which allows us to convert wavenumber k into its magnitude κ in (2.25). In particular, the resonance condition in k permits eight sign choices for k_1, k_2 and k_3 (for fixed positive k), but disregarding trivial pairings (e.g. $k = k_2$, $k_1 = k_3$; $k_1 = k_2$, $k = k_3$) leaves only four non-trivial cases where the integrand is non-zero. The resulting equation in κ is

$$\begin{aligned}\frac{\partial n_\kappa}{\partial t} = 4\pi \int |T_{k123}|^2 n_\kappa n_1 n_2 n_3 \left[\frac{1}{n_\kappa} + \frac{1}{n_1} - \frac{1}{n_2} - \frac{1}{n_3}\right] \delta(\omega_\kappa + \omega_1 - \omega_2 - \omega_3) \\ \times \big[\delta(\kappa + \kappa_1 - \kappa_2 + \kappa_3) + \delta(\kappa + \kappa_1 + \kappa_2 - \kappa_3) + \delta(\kappa - \kappa_1 - \kappa_2 - \kappa_3) \\ + \delta(\kappa - \kappa_1 + \kappa_2 + \kappa_3)\big] \,\mathrm{d}\kappa_1 \,\mathrm{d}\kappa_2 \,\mathrm{d}\kappa_3. \end{aligned} \tag{2.31}$$

We name the four terms in (2.31) I_1, I_2, I_3 and I_4, corresponding to the four delta functions in the square brackets. To further simplify I_1 associated with $\delta(\kappa + \kappa_1 - \kappa_2 + \kappa_3)$ in (2.31) (as an example), we notice that the frequency resonance condition can be reduced to (see Appendix D.1)

$$0 = \omega_\kappa + \omega_1 - \omega_2 - \omega_3 \approx \kappa_3 - \frac{\beta}{4}\kappa\kappa_1\kappa_2. \tag{2.32}$$

The wavenumber resonance condition is reduced to $\kappa + \kappa_1 - \kappa_2 + O(\beta) = 0$, with the $O(\beta)$ term negligible at leading order. Therefore, integrating out the frequency condition and using (2.30) reduces I_1 to

https://doi.org/10.1017/jfm.2026.11872 Published online by Cambridge University Press

$$I_1 = \int \left|\frac{3\alpha^2}{128}\sqrt{\beta}\kappa\kappa_1\kappa_2\right|^2 n_\kappa n_1 n_2 n_3 \left[\frac{1}{n_\kappa}+\frac{1}{n_1}-\frac{1}{n_2}-\frac{1}{n_3}\right]\delta(\kappa+\kappa_1-\kappa_2)\,\mathrm{d}\kappa_1\,\mathrm{d}\kappa_2. \tag{2.33}$$

Following similar procedures, we can reduce I_2 and I_3 to

$$I_2 = \int \left|\frac{3\alpha^2}{128}\sqrt{\beta}\kappa\kappa_1\kappa_3\right|^2 n_\kappa n_1 n_2 n_3 \left[\frac{1}{n_\kappa}+\frac{1}{n_1}-\frac{1}{n_2}-\frac{1}{n_3}\right]\delta(\kappa+\kappa_1-\kappa_3)\,\mathrm{d}\kappa_1\,\mathrm{d}\kappa_3 \tag{2.34}$$

and

$$I_3 = \int \left|\frac{3\alpha^2}{128}\sqrt{\beta}\kappa\kappa_2\kappa_3\right|^2 n_\kappa n_1 n_2 n_3 \left[\frac{1}{n_\kappa}+\frac{1}{n_1}-\frac{1}{n_2}-\frac{1}{n_3}\right]\delta(\kappa-\kappa_2-\kappa_3)\,\mathrm{d}\kappa_2\,\mathrm{d}\kappa_3, \tag{2.35}$$

respectively. For I_4, the frequency condition cannot be satisfied for $\kappa \sim O(1)$, thus $I_4 = 0$ and does not contribute to (2.31).

Integrals (2.33)–(2.35) can be further simplified depending on the size of n_κ at $\kappa \sim \beta$ relative to n_κ in the inertial range. Here, the notation $\kappa \sim \beta$ refers to the low-wavenumber range where n_κ is evaluated, not to the scaling of the wavenumbers retained in the reduced resonance condition. In what follows, we discuss two cases: Cases A and B with n_κ respectively small and large in the vicinity of $\kappa \sim \beta$. These two cases physically correspond to situations with and without large-scale damping in the simulations demonstrated in § 3.2.2.

2.2.1. *Case A*

Consider I_1 with $n_3 \ll n_\kappa, n_1, n_2$. The integral in (2.33) can be reformulated as (with $1/n_3$ term dominating over other terms in the square bracket)

$$I_1 = -\int \left|\frac{3\alpha^2}{128}\sqrt{\beta}\kappa\kappa_1\kappa_2\right|^2 n_\kappa n_1 n_2 \delta(\kappa+\kappa_1-\kappa_2)\,\mathrm{d}\kappa_1\,\mathrm{d}\kappa_2. \tag{2.36}$$

Similar procedures applied to I_2 and I_3 reduce (2.34) and (2.35) to

$$I_2 = -\int \left|\frac{3\alpha^2}{128}\sqrt{\beta}\kappa\kappa_1\kappa_3\right|^2 n_\kappa n_1 n_3 \delta(\kappa+\kappa_1-\kappa_3)\,\mathrm{d}\kappa_1\,\mathrm{d}\kappa_3 \tag{2.37}$$

and

$$I_3 = \int \left|\frac{3\alpha^2}{128}\sqrt{\beta}\kappa\kappa_2\kappa_3\right|^2 n_\kappa n_2 n_3 \delta(\kappa-\kappa_2-\kappa_3)\,\mathrm{d}\kappa_2\,\mathrm{d}\kappa_3. \tag{2.38}$$

By defining

$$R_{12}^{\kappa} = \left|\frac{3\alpha^2}{128}\sqrt{\beta}\kappa\kappa_1\kappa_2\right|^2 n_\kappa n_1 n_2 \delta(\kappa-\kappa_2-\kappa_1) \tag{2.39}$$

the integral I can be expressed as

$$I = I_1 + I_2 + I_3 = \int \left(R_{12}^{\kappa} - R_{1\kappa}^{2} - R_{\kappa 2}^{1}\right)\mathrm{d}\kappa_1\,\mathrm{d}\kappa_2. \tag{2.40}$$

https://doi.org/10.1017/jfm.2026.11872 Published online by Cambridge University Press

After applying the Zakharov transformations (Zakharov *et al.* 2012) and assuming a solution ansatz $n_\kappa \sim \kappa^{-x}$ (see Appendix D.2 for full details), we can write (2.40) as

$$I = \int R_{12}^{\kappa} \left[1 - \left(\frac{\kappa_1}{\kappa}\right)^{3x-8} - \left(\frac{\kappa_2}{\kappa}\right)^{3x-8} \right] \mathrm{d}\kappa_1 \, \mathrm{d}\kappa_2. \tag{2.41}$$

The condition for a stationary solution is obtained by requiring the bracketed term to vanish, which leads to

$$3x - 8 = 1 \Rightarrow x = 3, \tag{2.42}$$

which is the KZ exponent for Case A with small n_κ at $\kappa \sim \beta$.

In Appendix D.4, we further provide a locality analysis which leads to a locality window of $5/2 < x < 4$. The solution $x = 3$ is therefore within the locality window and represents a valid local solution to the WKE.

2.2.2. *Case B*

Considering $n_3 \gg n_\kappa, n_1, n_2$ for I_1 and similar conditions for I_2 and I_3, integrals (2.33)–(2.35) are reduced to

$$I_1 = \int \left| \frac{3\alpha^2}{128} \sqrt{\beta} \kappa \kappa_1 \kappa_2 \right|^2 n_\kappa n_1 n_2 n_3 \left[\frac{1}{n_\kappa} + \frac{1}{n_1} - \frac{1}{n_2} \right] \delta(\kappa + \kappa_1 - \kappa_2) \, \mathrm{d}\kappa_1 \, \mathrm{d}\kappa_2, \tag{2.43}$$

$$I_2 = \int \left| \frac{3\alpha^2}{128} \sqrt{\beta} \kappa \kappa_1 \kappa_3 \right|^2 n_\kappa n_1 n_2 n_3 \left[\frac{1}{n_\kappa} + \frac{1}{n_1} - \frac{1}{n_3} \right] \delta(\kappa + \kappa_1 - \kappa_3) \, \mathrm{d}\kappa_1 \, \mathrm{d}\kappa_3 \tag{2.44}$$

and

$$I_3 = \int \left| \frac{3\alpha^2}{128} \sqrt{\beta} \kappa \kappa_2 \kappa_3 \right|^2 n_\kappa n_1 n_2 n_3 \left[\frac{1}{n_\kappa} - \frac{1}{n_2} - \frac{1}{n_3} \right] \delta(\kappa - \kappa_2 - \kappa_3) \, \mathrm{d}\kappa_2 \, \mathrm{d}\kappa_3. \tag{2.45}$$

Defining

$$R_{12}^{\kappa} = \left| \frac{3\alpha^2}{128} \sqrt{\beta} \kappa \kappa_1 \kappa_2 \right|^2 n_\kappa n_1 n_2 n_3 \left[\frac{1}{n_\kappa} - \frac{1}{n_2} - \frac{1}{n_1} \right] \delta(\kappa - \kappa_2 - \kappa_1), \tag{2.46}$$

and applying the Zakharov transformations with the solution ansatz $n_\kappa \sim \kappa^{-x}$ (see Appendix D.3 for full details), we arrive at

$$I = \int R_{12}^{\kappa} \left[1 - \left(\frac{\kappa_1}{\kappa}\right)^{6x-8} - \left(\frac{\kappa_2}{\kappa}\right)^{6x-8} \right] \mathrm{d}\kappa_1 \, \mathrm{d}\kappa_2. \tag{2.47}$$

By enforcing the same condition as in § 2.2.1, we find that the stationary solution is obtained at

$$6x - 8 = 1 \Rightarrow x = \frac{3}{2}, \tag{2.48}$$

which is the KZ exponent for Case B with large n_κ at $\kappa \sim \beta$. The locality analysis in Appendix D.4 shows a locality window of $4/3 < x < 5/2$, so that this KZ solution is local.

3. Numerical study

A subsequent numerical study is performed with the purpose of verifying the theoretical results derived in § 2. In this section, we begin by outlining the methodology and numerical set-up implemented in this study. We then discuss the results from two scenarios, namely free-evolution and forced-dissipated configurations.

https://doi.org/10.1017/jfm.2026.11872 Published online by Cambridge University Press

3.1. *Methodology*

We simulate the KB system (2.4) and (2.5) using a pseudospectral method paired with a fourth-order Runge–Kutta time marching scheme with an integration factor (IF-RK4) formulation (e.g. Pan 2020). Key details of the scheme can be found in Appendix G, along with a validation against existing exact solutions of the KB system. All numerical experiments are performed on a computational domain of size $L = 2\pi$ with periodic boundary conditions, discretised using $N = 4096$ free wave modes (before de-aliasing). The value of β is correspondingly chosen (and specified in each subsection) such that the high-order term in the dispersion relation in (2.8) is much smaller than the linear term, even for the highest wavenumber. In this section, we further present details of the numerical set-up for the free-evolution and forced-dissipated cases in §§ 3.2.1 and 3.2.2, respectively. We then introduce the formulation of the direct scattering transform (DST), as well as the numerical strategies to solve the spectral problem for the purpose of testing isospectrality for the KB model associated with its integrability.

3.1.1. *Free-evolution configuration*

All freely evolving cases are performed without external forcing and damping, using a Gaussian spectrum $S(\kappa)$ as the initial condition (e.g. Pelinovsky & Sergeeva (Kokorina) 2006; Flamarion & Pelinovsky 2024):

$$S(\kappa) = Q \exp\left(- \frac{(\kappa - \kappa_p)^2}{2K^2} \right), \tag{3.1}$$

where $\kappa_p = 512$ represents the wavenumber peak, $K = 51.2$ characterises the spectral bandwidth and Q is chosen such that the resulting data size is $\lesssim 1$ (say measured by $||\hat{\eta}_\kappa||_\infty$ and $||\hat{u}_\kappa||_\infty$). The amplitude of each Fourier component $\hat{\eta}_\kappa$ is drawn from the spectrum $S(\kappa)$. To construct a bidirectional field, $\hat{\eta}_\kappa$ is evenly split to equally distribute energy between left- and right-propagating components. Each component is assigned a random phase drawn uniformly from $(0, 2\pi]$. The component $\hat{u}_\kappa$ is then obtained from η_κ for both left- and right-propagating components via the linear relation. For all free-evolution experiments, we fix the dispersion parameter $\beta = 0.2$, and vary the nonlinearity parameter α to control the nonlinearity level.

3.1.2. *Forced-dissipated configuration*

All experiments begin from a quiescent initial state. Waves are excited by a forcing term $F(\kappa, t)$ added to the right-hand side of (2.5) (or (2.7) defined in the spectral domain), in the form of (e.g. Dyachenko *et al.* 2004; Pan 2020; Zhang & Pan 2022*b*; Korotkevich 2023)

$$F(\kappa, t) = \begin{cases} f_\kappa \exp\big[- Ct + i(\omega_\kappa t + R)\big], & t \leqslant T_c, \\ f_\kappa \exp\big[- CT_c + i(\omega_\kappa t + R)\big], & t > T_c, \end{cases} \tag{3.2}$$

with

$$f_\kappa = \begin{cases} f_0 \dfrac{(\kappa - \kappa_1)(\kappa_2 - \kappa)}{(\kappa_1 - \kappa_2)^2}, & \kappa_1 \leqslant \kappa \leqslant \kappa_2, \\ 0, & \text{otherwise}, \end{cases} \tag{3.3}$$

where $f_0 = 0.88$ controls the forcing amplitude (leading to a solution of size $O(1)$ and mitigating the finite-size effect; e.g. L'vov & Nazarenko 2010; Hrabski & Pan 2020; Zhang & Pan 2022*a*), $\kappa_1 = 26$ and $\kappa_2 = 38$ define the lower and upper bounds of the

https://doi.org/10.1017/jfm.2026.11872 Published online by Cambridge University Press

forcing band and R is a uniformly distributed random number in the interval $(0, 2\pi]$. As defined in (3.2), the forcing amplitude decays exponentially at rate C for $t < T_c$ and remains constant for $t \geqslant T_c$. Such an implementation allows for a stationary state of the system to be achieved faster (Zhang & Pan 2022*b*). For this study, we set $T_c = 500T_p$ and $C = \ln 5/T_c$, where T_p is the peak period (computed using $\kappa_p = (\kappa_1 + \kappa_2)/2 = 32$).

To account for dissipation at small scales, we add terms $D_1\hat{\eta}_\kappa$ and $D_1\hat{u}_\kappa$ to (2.4) and (2.5), respectively. The dissipation coefficient takes the form (e.g. Dyachenko *et al.* 2004; Korotkevich 2023)

$$D_1(\kappa) = \nu_1(\kappa - \kappa_{d_1})^2, \qquad \kappa \geqslant \kappa_{d_1}, \tag{3.4}$$

where $\nu_1 = 10^{-4}$ controls the dissipation strength and $\kappa_{d_1} = 900$ is the onset wavenumber. To distinguish Cases A and B, we introduce a hypo-viscous damping term at large scales only for Case A, with the coefficient in the form of

$$D_2(\kappa) = \nu_2\kappa^{-4}, \qquad \kappa \leqslant \kappa_{d_2}, \tag{3.5}$$

where $\nu_2 = 5 \times 10^{-6}$. When (3.5) is applied, it introduces damping that suppresses n_κ at large scales, consistent with the assumption in Case A. Without this damping, the inverse cascade fills in large scales, causing n_k to grow large in the simulation, consistent with Case B. In all forced-dissipated cases, we fix $\alpha = 0.0001$ and $\beta = 0.001$, so that the validity condition of normal-form transformation is satisfied together with $O(1)$ solution size.

3.1.3. *Direct scattering transform*

In this study, we utilise the DST as a diagnostic tool. Since the KB system is completely integrable, it admits a Lax pair. We focus on the spectral problem alone, which suffices for the solution of DST. At each time instant, the spectral problem for the system is given by Kaup (1975)

$$\Psi_{xx} + \left[k^2 + \frac{3}{4}\beta^{-1} + ikq(x) + r(x)\right]\Psi = 0, \tag{3.6}$$

where k is the eigenvalue, Ψ is the eigenfunction and $q(x)$ and $r(x)$ are potentials defined as

$$q(x) = \frac{\sqrt{3}}{2}\alpha\beta^{-1/2}u(x), \quad r(x) = \frac{3}{4}\alpha\beta^{-1}\left(\eta(x) - \frac{1}{4}\alpha u(x)^2\right), \tag{3.7}$$

which are assumed to decay to zero at $|x| \to \infty$. Solving the DST problem (3.6) amounts to finding the eigenvalue k and its corresponding eigenfunction Ψ. The property of the solution depends critically on the spectral parameter defined by $E(k) = \{k^2 + 3/(4\beta)\}^{1/2}$. However, $E(k)$ is a multivalued function in the complex plane of k, and involves branch points at $k = \pm i\sqrt{3/(4\beta)}$ (more precisely, when a closed loop around $\pm i\sqrt{3/(4\beta)}$ is followed, $E(k)$ changes its value as the loop returns to the original point). Since it is inconvenient to work with a branch point, it is a conventional practice to perform a conformal transformation to the ζ plane to eliminate these branch points (Kaup 1975). The transformation is defined by

$$k = \frac{1}{4}\left(\zeta - \frac{B}{\zeta}\right), \qquad E = \frac{1}{4}\left(\zeta + \frac{B}{\zeta}\right) \tag{3.8}$$

with $B = 3/\beta$ so that $E(\zeta) = \{k(\zeta)^2 + 3/(4\beta)\}^{1/2}$ as defined above. The spectral problem (3.6) can now be written as

$$\Psi_{xx} + \left[E(\zeta)^2 + ik(\zeta)q(x) + r(x)\right]\Psi = 0, \tag{3.9}$$

https://doi.org/10.1017/jfm.2026.11872 Published online by Cambridge University Press

where both k and E are single-valued in ζ. We have now circumvented the multivalued function and branch points that are associated with working in the k plane. As a result, the transformation $\zeta \mapsto -B/\zeta$ changes the sign of E, $E \mapsto -E$, and leaves both k and E^2 invariant. Therefore, each ζ solution of (3.9) has a 'mirror' part of $-B/\zeta$, and we plot in the result section only the one corresponding to the upper half E plane, i.e. with $\mathrm{Im}[E(\zeta)] > 0$ (see caption of figure 2 for details).

Referring to (3.9) again, we see that a continuous spectrum is characterised by $\mathrm{Im}[E(\zeta)] = 0$, since at $|x| \to \infty$, it corresponds to an oscillatory solution of $\Psi(x)$. This solution occurs when ζ is either purely real or lies on the curve defined by $|\zeta| = \sqrt{3/\beta}$, as described in the caption of figure 2. We are interested in the discrete spectrum of eigenvalues that are away from the continuous spectrum, physically corresponding to bound states (or solitons).

The detailed numerical procedure to solve (3.9) is described in Appendix H. We further remark that the traditional DST procedure assumes the problem to be defined on $\mathbb{R}$, but our numerical solutions of $u(x)$ and $\eta(x)$ are periodic. For this reason, the DST may not be precise; nevertheless, it remains an effective tool for identifying bound states of the solution (see Colléaux *et al.* (2025) for similar applications). In practice, this problem requires us to handle some spurious eigenvalues using a specific criterion detailed in Appendix H.

3.2. *Results*

3.2.1. *Free-evolution experiments*

We start by examining a free-evolution case for the full dispersion relation (2.8) with $\alpha = 0.2$ (and $\beta = 0.2$ for all cases in this section as presented in § 3.1.1), which corresponds to a traditional regime with dispersion balancing nonlinearity. Figure 1 shows the evolution of the system from an initial Gaussian spectrum to the stationary spectrum evaluated at $t = 2 \times 10^6 T_p$. It is clear that the wavenumber spectrum exhibits significant evolution, ultimately reaching a state consistent with the RJ scaling, $n_\kappa \sim \kappa^{-1}$. We note, however, that the observed RJ-like spectrum should be distinguished from the classical RJ distribution in wave turbulence theory, as it does not exhibit universality across the full spectral range when the spectrum is peaked at large scales (see Appendix E). Figure 2 presents the corresponding discrete eigenvalue spectrum obtained via the DST at the beginning and end of the simulation (we note that the identification of bound states in a random wave background of high nonlinearity is also found in Colléaux *et al.* (2025)). Aside from some very minor drift attributed to the periodic domain (in contrast to the unbounded domain $\mathbb{R}$ assumed in theory), all eigenvalues remain essentially constant throughout the long-time evolution, consistent with the isospectral property of the integrable system. This case therefore provides clear evidence that complete integrability does not guarantee a frozen wavenumber spectrum, as substantial spectral evolution can still occur.

We next study the spectral evolution for several values of α, in order to cover a broad range of nonlinearity. Figure 3 shows the spectral evolution for $\alpha = 0.2$, 0.04 and 0.02. We see that for all cases, the spectrum evolves into the same RJ state, although the corresponding evolution time differs (specifically, spectra are shown at $5 \times 10^5 T_p$, $8 \times 10^5 T_p$ and $1.2 \times 10^6 T_p$ for the three cases). This spectral phenomenon has also been observed in numerical simulations of the KdV equation (Pelinovsky & Sergeeva (Kokorina) 2006). In both cases, we suspect it arises from quasi-resonant three-wave interactions. To assess whether such interactions are relevant, we evaluate the bi-coherence defined as (Pan & Yue 2017)

https://doi.org/10.1017/jfm.2026.11872 Published online by Cambridge University Press

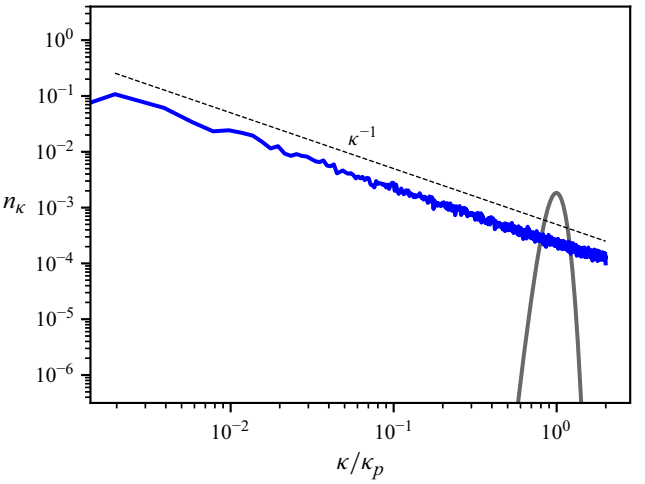


Figure 1. Initial (solid grey) and stationary (solid blue) spectra at $t = 0$ and $t = 2 \times 10^6 T_p$ for the free-evolution case with $\alpha = \beta = 0.2$. The RJ scaling is marked (dashed black line).

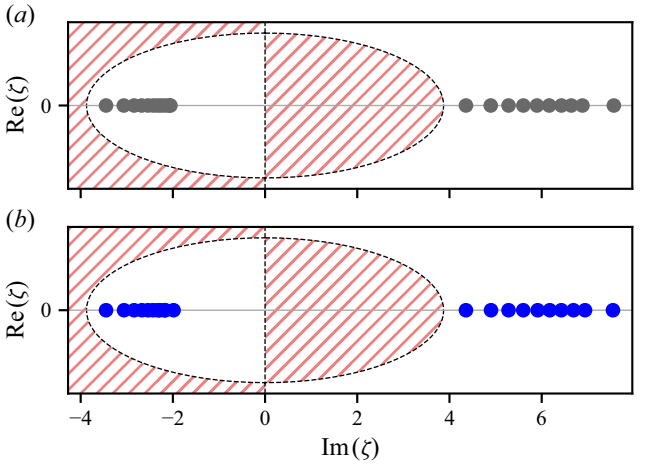


Figure 2. The spectrum of discrete eigenvalues ζ (blue and grey points) obtained via DST at (*a*) $t = 0$ and (*b*) $t \approx 2 \times 10^6 T_p$, corresponding to the times of initial and stationary spectra in figure 1. The lower half E plane (i.e. where $\mathrm{Im}[E(\zeta)] < 0$) is marked by the red hatched region and the continuous-spectrum region (i.e. where $\mathrm{Im}[E(\zeta)] = 0$) is marked by the dashed black line.

$$B(\kappa, \kappa_1) = \frac{|\langle \eta_\kappa^* \eta_{\kappa_1} \eta_{\kappa_2 = \kappa - \kappa_1} \rangle|}{\langle |\eta_\kappa| |\eta_{\kappa_1}| |\eta_{\kappa_2 = \kappa - \kappa_1}| \rangle}, \tag{3.10}$$

where η_κ is the Fourier component of the surface elevation obtained from numerical simulation and $\langle \cdots \rangle$ denotes a time average over the stationary data. The bi-coherence function $B(\kappa, \kappa_1)$ varies between 0 and 1, with 1 and 0 corresponding to perfect and no correlation, respectively. Given a set of discrete wavenumbers, B obtains a high value for quasi-resonances. We compute $B(\kappa, \kappa_1)$ over all (κ, κ_1) drawn from the discrete numerical grid. Figures 4(*a*) and 4(*b*) show the bi-coherence plots for high ($\alpha = 0.2$) and low ($\alpha = 0.02$) nonlinearity cases, respectively. In both cases, the analysis shows values of

https://doi.org/10.1017/jfm.2026.11872 Published online by Cambridge University Press

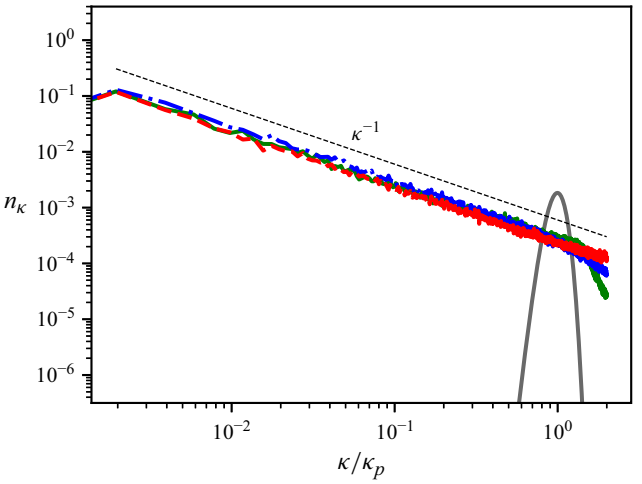


Figure 3. The initial spectrum (solid grey) and stationary spectra with $\alpha = 0.2$ (dashed red), $\alpha = 0.04$ (dash-dot blue) and $\alpha = 0.02$ (solid green), respectively taken at $5 \times 10^5 T_p$, $8 \times 10^5 T_p$ and $1.2 \times 10^6 T_p$. The RJ scaling is marked (dashed black).

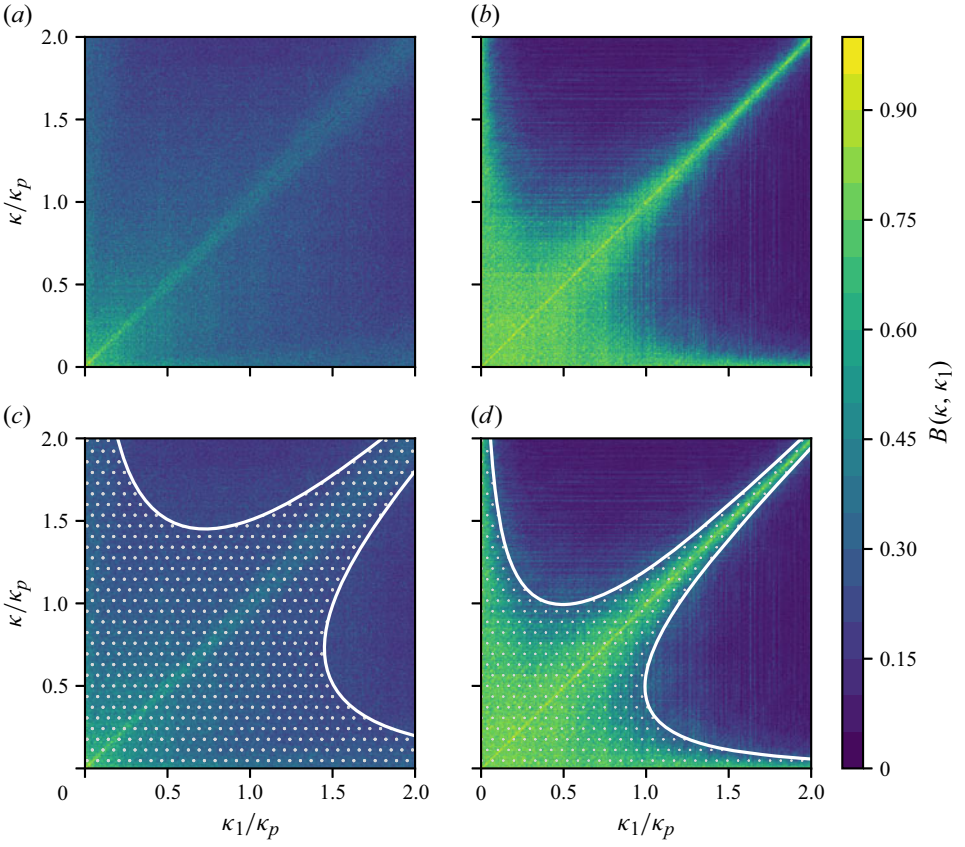


Figure 4. Bi-coherence $B(\kappa, \kappa_1)$ for (a,c) $\alpha = 0.2$ and (b,d) $\alpha = 0.02$. Panels (a,b) show the full bi-coherence distribution, while panels (c,d) highlight the corresponding quasi-resonant regions. The solid white line marks the frequency-mismatch threshold $\Delta\omega = 0.08$ for $\alpha = 0.2$ and $\Delta\omega = 0.025$ for $\alpha = 0.02$, chosen such that the region enclosed (white dots) accounts for 80 % of the total bi-coherence.

https://doi.org/10.1017/jfm.2026.11872 Published online by Cambridge University Press

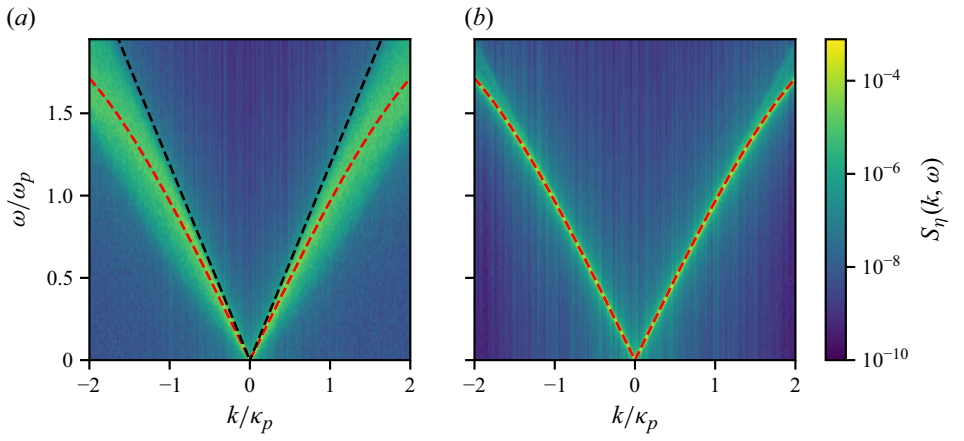


Figure 5. The k–ω spectra $S_\eta(k,\omega)$ for (a) $\alpha = 0.2$ and (b) $\alpha = 0.02$. The KB dispersion relation (2.8) is denoted by the dashed red line and the soliton dispersion relation (for the most dominant bound state) is marked by the dashed black line in (a).

B that are well above zero, confirming quasi-resonant triads across nonlinearity regimes. To robustly assess the nonlinearity dependence, we compute the frequency mismatch $\Delta\omega$

$$|\omega(\kappa) - \omega(\kappa_1) - \omega(\kappa_2)| \leqslant \Delta\omega \tag{3.11}$$

for each discrete triad. Detailed examples of near-resonant interactions and resonance broadening on discrete grids are provided for triads in Dyachenko *et al.* (2003) and for quartets in Korotkevich *et al.* (2016). For each case, we then determine the value of $\Delta\omega$ for which the cumulative bi-coherence of the triads satisfying (3.11) accounts for 80 % of the total bi-coherence, and mark this threshold directly on the corresponding plot. Figure 4(c) demonstrates that the high nonlinearity enables quasi-resonant interactions across larger mismatches, as the allowable frequency mismatch $\Delta\omega$ grows with nonlinear broadening (evident in figure 5a). In contrast, the low-nonlinearity case shown in figure 4(d) confines the quasi-resonances to a smaller frequency mismatch $\Delta\omega$. This confirms that quasi-resonant triads, active across all α regimes considered, drive the spectral evolution observed in this section.

We further remark that the spectral evolution towards $n_\kappa \sim \kappa^{-1}$ is also observed in experiments of bidirectional shallow-water waves, but it is often attributed to the soliton dynamics (e.g. Redor *et al.* 2019, 2021; Leduque *et al.* 2025). To assess the influence of solitons in our study, we plot the wavenumber–frequency (k–ω) spectra from two representative simulations corresponding to the largest and smallest values of α in figure 5. We find that the energy branch in the k–ω spectra closely follows the free-wave dispersion relation (2.8), rather than the soliton dispersion relation marked in the figure. For the case with the largest $\alpha = 0.2$, the soliton energy identified by the DST can be computed and found to only constitute 3 % of the total energy, which is masked by the nonlinear broadening in figure 5(a). It is therefore safe to conclude that the observed RJ spectral state is caused by interactions among random free waves, rather than by soliton dynamics.

3.2.2. *Forced-dissipated experiments*

We now investigate the forced-dissipated cases of the non-integrable Boussinesq equation. In this section, we use $\alpha = 0.0001$ and $\beta = 0.001$, ensuring that we operate in a regime where the normal-form transformation is valid and quartet interactions play a significant

https://doi.org/10.1017/jfm.2026.11872 Published online by Cambridge University Press

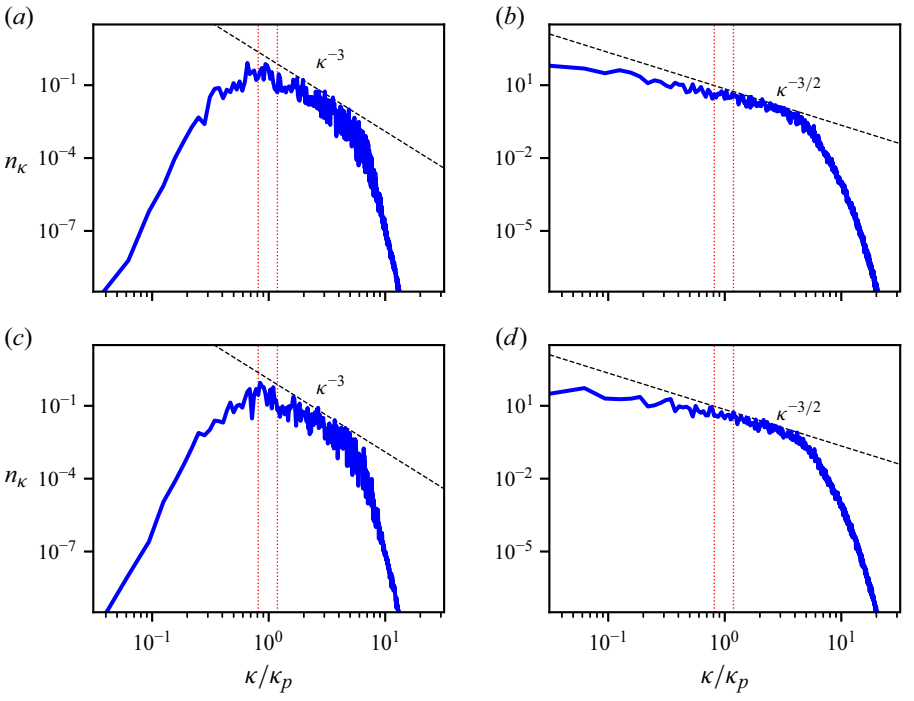


Figure 6. Stationary wave action spectra for the truncated-dispersion system (a,b) and the full KB system (c,d). (a,c) Case A with theoretical scaling $n_\kappa \sim \kappa^{-3}$. ($b$,$d$) Case B with theoretical scaling $n_\kappa \sim \kappa^{-3/2}$. The forcing range is indicated by the dotted red lines, and the corresponding theoretical scalings are marked by the dashed black lines.

role in the spectral evolution towards small scales (see further discussion in Appendix F). We first present results with the presence of large-scale damping, corresponding to Case A in the theoretical derivation. Figure 6(a) shows the stationary spectrum after an evolution time of $6 \times 10^5 T_p$, where large scales contain minimal energy as desired. We see an inertial range slightly exceeding 2/3 of a decade with a slope close to the theoretical prediction of κ^{-3}. Without large-scale damping, the resulting stationary spectrum corresponds to Case B with sufficiently high energy at large scales, as shown in figure 6(b). To the right of the forcing range, the stationary spectrum spans approximately 2/3 of a decade and shows a tendency towards the theoretical scaling of $\kappa^{-3/2}$ for Case B.

We note that the inertial range in our numerical simulations is comparatively short relative to that of other wave turbulence studies. Increasing the scale separation in these simulations is not a trivial task and is delicate in practice. To increase κ_{max}, one must decrease β to ensure $(\beta/3)\kappa_{max}^2 \ll 1$. At the same time, we require $\alpha \ll \beta$ to remain in the relevant four-wave interaction regime. However, α cannot be too small, as discrete effects then become significant.

We remark that the results presented in this section differ substantially from the forced bidirectional shallow-water wave experiments in Redor *et al.* (2019, 2021) and Leduque *et al.* (2025). In these experiments, the system nonlinearity, measured by α/β, is high enough to induce the formation of a large number of solitons (i.e. soliton gas), which manifests itself as an exponentially decaying energy spectrum at moderate to small scales. In our study, α/β is kept low, suppressing the formation of solitons. This is confirmed by

https://doi.org/10.1017/jfm.2026.11872 Published online by Cambridge University Press

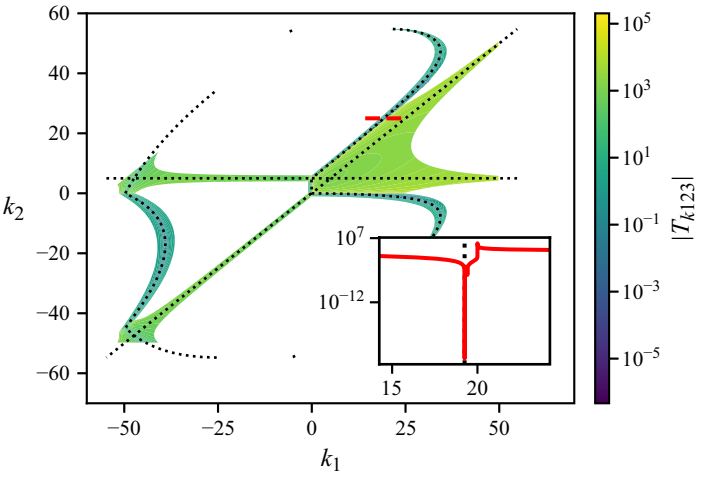


Figure 7. Interaction coefficient T_{k123} for $\beta = 0.001$, $k = 5.0$, restricted to $|\Delta\omega| \leqslant 2$ near the KB resonant manifold. The dotted black lines mark $\Delta\omega = 0$ curves: the curved branch is the KB resonant manifold, while the diagonal and horizontal branches correspond to trivial resonances. The inset shows a cross-section taken along the dashed red line, illustrating the behaviour of the coefficient across the resonant manifold.

DST showing no bound state content in the system. Therefore, the observed power-law KZ scalings arise solely from interactions of free random waves.

4. Discussion and conclusion

In this work, we establish the wave turbulence theory for 1-D bidirectional shallow-water waves derived from Boussinesq-type equations. We show that for the full KB equation, the four-wave interaction coefficient vanishes on the resonant manifold, as expected from integrability. However, when considering a truncated dispersion relation representative of non-integrable Boussinesq models, we are able to derive a robust, non-trivial WKE as well as its KZ solutions.

Numerical simulations in this work highlight the significant spectral evolution that can be triggered by either quasi-resonant triad interactions or truncating the dispersion relation, which in turn breaks the integrability of the system. A closer examination of our results reveals that quasi-resonant quartet interactions may play a role in driving the kinetic behaviour, even in the full KB model. This may seem counterintuitive as it contradicts the empirical belief that integrable models do not yield kinetic behaviour. In the following, we briefly present two pieces of evidence, followed by a discussion of the mechanism.

The first piece of evidence comes from a set of free-evolution simulations of the full KB equation. In Appendix F, we provide identical simulations of the KdV equations, derived from KB by eliminating one direction of propagation (thus prohibiting four-wave interactions). For larger values of α (i.e. $\alpha = 0.2$), the KdV simulation exhibits relaxation towards the RJ spectral state on the same time scale as the KB simulation, which can be attributed to the quasi-resonant triad interactions. However, for smaller values of α (i.e. $\alpha = 0.02$), only the KB simulation exhibits propagation of the RJ scaling towards small scales. This illustrates that quasi-resonant quartet interactions must play a role, since exact resonances vanish on the resonant manifold.

The second piece of evidence comes from the forced-dissipated simulations. We find that even for the full KB equation, the spectrum evolves into a power-law state that appears

https://doi.org/10.1017/jfm.2026.11872 Published online by Cambridge University Press

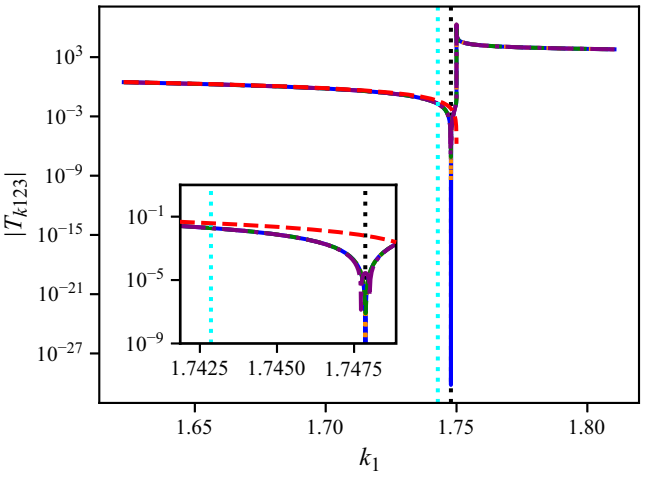


Figure 8. Interaction coefficients T_{k123} for $\beta = 0.001$, $k = 1.5$ and $k_2 = 3.25$, evaluated using the KB dispersion relation (solid blue) and truncated dispersion relations with $O(\beta^3)$ corrections (dotted orange), $O(\beta^2)$ corrections (dashed green) and $O(\beta)$ corrections (dash-dotted purple). Also shown are the analytical coefficient (2.27*a*) (dashed red), the KB resonant manifold (dotted black) and the contour $|\Delta\omega| = 0.01$ (dotted cyan). The inset magnifies the behaviour near the resonant manifold.

to be consistent with both cases of the truncated-dispersion model (shown in figures 6*c* and 6*d*). This result is curious, as integrable models are not expected to exhibit significant spectral evolution due to the absence of wave kinetics. Since the values of α and β are chosen to correspond to a regime where four-wave interactions are relevant, quasi-resonant quartet interactions likely play a significant role here.

To better understand the mechanism, we examine the behaviour of T_{k123} near the resonant manifold, as shown in figure 7. In particular, the inset of the figure shows T_{k123} along a section across the resonant manifold. We observe 'near-singular' behaviour in the sense that the coefficient drops sharply to zero on the resonant manifold, but quickly rises to significant finite values nearby. This implies that in the discrete setting with finite nonlinearity, even a minimal shift from the resonant manifold may allow quasi-resonant interactions to emerge as the primary mechanism for spectral evolution, while exact resonances may play a negligible role. We provide further insight in figure 8 by comparing T_{k123} evaluated using the full KB dispersion relation with evaluations from truncated-dispersion approximations retaining successively higher-order terms. The figure also includes the analytical expression given by T_I in (2.27*a*). We see that T_{k123} exhibits sharp minima on the resonant manifold, with each successive truncated-dispersion evaluation lying closer to the full KB result as higher-order dispersive corrections are retained. However, the truncated coefficients no longer exhibit the exact cancellation of constituent terms associated with integrability. Slightly off the resonant manifold ($|\Delta\omega| = 0.01$), all coefficients are well described by the analytical expression. This small but finite frequency mismatch regime is most relevant for our numerical simulations (both full and truncated), since the discrete grid captures near- rather than exact-resonant interactions, and finite-amplitude nonlinear broadening allows interactions with small frequency mismatches to contribute. It is therefore unsurprising that the KB and non-integrable Boussinesq models produce the same KZ state in the present simulations, as this near-resonant regime reflects the behaviour of the interaction coefficient in the vicinity of the resonant manifold, where both coefficients coincide with the analytical expression. The dominant role of

https://doi.org/10.1017/jfm.2026.11872 Published online by Cambridge University Press

quasi-resonant interactions is consistent with examples from previous numerical studies of the Zakharov equation (Annenkov & Shrira 2006) and the Majda–McLaughlin–Tabak equation (Hrabski & Pan 2020). This is further supported by Banks *et al.* (2022), who demonstrate that a good approximation of a dynamical equation by a WKE requires the number of quasi-resonances to be significantly larger than the number of exact resonances.

A deeper question is whether numerical simulations can accurately represent the kinetic limit. The 'ideal' kinetic regime associated with the formal derivation of the WKE assumes $L \to \infty$ and $\epsilon \to 0$. Numerical studies have been performed to probe the kinetic limit (e.g. Hrabski & Pan 2024), demonstrating convergence to WKE predictions as the corresponding limits are approached. In this context, the observed kinetic behaviour in our numerical experiments should be interpreted as that of a finite-amplitude, finite-box regime, rather than as evidence that the integrable and non-integrable systems are equivalent in the formal kinetic limit.

This work challenges the traditional view that there is no wave turbulence in the shallow-water setting. Quasi-resonances drive the kinetic behaviour in both the integrable KB and non-integrable models, aligning the former more closely with the traditional wave-turbulence framework and motivating further study of other integrable systems. A theoretical formulation of this kinetic behaviour and its analytical derivation are left for future work.

Acknowledgements. The authors thank Professor M. Onorato for his valuable insights and feedback on the interaction coefficient calculation, which substantially strengthened this work. In particular, he provided notes and code for the calculation of the KB coefficient, which helped us identify and correct an error in an early version of the manuscript.

Funding. This research was supported by the Simons Foundation (Award ID no. 651459). The computation was performed on the Great Lakes HPC Cluster provided by Advanced Research Computing (ARC) at the University of Michigan, Ann Arbor.

Declaration of interests. The authors report no conflict of interest.

Appendix A. Validity condition for the normal-form transformation

We consider a spectrum (see figure 9) with finite bandwidth $\Delta = k^+ - k^-$, containing $N_\Delta = \Delta L/(2\pi)$ modes in Δ. We make the following assumptions:

(i) the spectrum decays sufficiently fast outside $[k^-, k^+]$;
(ii) everything is comparable in the range $[k^-, k^+]$, i.e. $k^+ = C_1 k^-$, $\max(n(k)) = C_2 \min(n(k))$ for some constants C_1 and C_2.

We note that assumption (i) is necessary to eliminate singularities arising from large wavenumbers in the normal-form transformation, as elaborated later in this appendix. Our objective is to derive a condition under which (2.24) holds for $k \in p\mathbb{Z}$, where $p = 2\pi/L$. For this purpose, let us consider the most singular terms on the left-hand side, i.e. those for which the denominators are of $O(\beta)$ rather than $O(1)$. For example, we take three wavenumbers in $\Gamma^{[1]}$ to be all positive, with $\omega_k - \omega_1 - \omega_2 \sim \beta k k_1 k_2$ in the first term and $\omega_k + \omega_1 - \omega_2 \sim \beta k k_1 k_2$ in the second term. Additionally, since $\omega_k + \omega_1 + \omega_2 \sim O(1)$ always holds, the third term can be neglected. Putting everything together, we have

https://doi.org/10.1017/jfm.2026.11872 Published online by Cambridge University Press

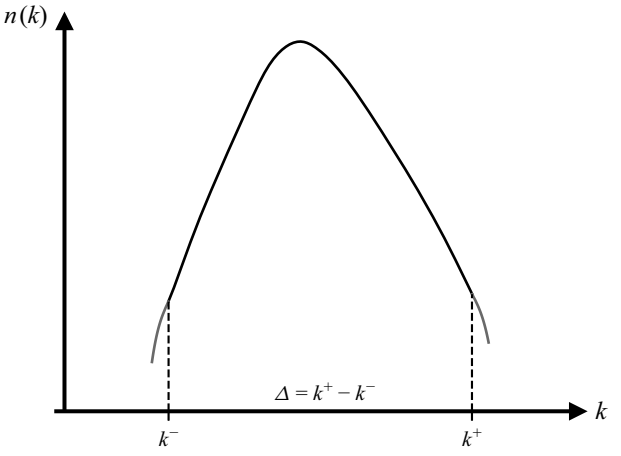


Figure 9. A sketch of the spectrum under consideration, with finite bandwidth Δ.

$$\begin{aligned}\text{Left-hand side} &\sim \Big| \sum_{k_1+k_2=k,all>0} \frac{\alpha(kk_1k_2)^{1/2}}{\beta kk_1k_2} b_{k_1}b_{k_2} - 2\sum_{k_1+k=k_2,all>0} \frac{\alpha(kk_1k_2)^{1/2}}{\beta kk_1k_2} b^*_{k_1}b_{k_2}\Big| \\ &\sim \Big| \sum_{k_1=p}^{k-p} \frac{\alpha}{\beta[kk_1(k-k_1)]^{1/2}} b_{k_1}b_{k-k_1} + \sum_{k_1=p}^{\infty} \frac{\alpha}{\beta[kk_1(k+k_1)]^{1/2}} b^*_{k_1}b_{k+k_1}\Big| \\ &\sim \Big| \underbrace{\sum_{k_1=p}^{k-p} \frac{\alpha}{\beta[kk_1(k-k_1)]^{1/2}} b_{k_1}b_{k-k_1}}_{①} + \underbrace{\sum_{k_1=p}^{k-p} \frac{\alpha}{\beta[kk_1(k+k_1)]^{1/2}} b^*_{k_1}b_{k+k_1}}_{②} \\ &\quad + \underbrace{\sum_{k_1=k}^{\infty} \frac{\alpha}{\beta[kk_1(k+k_1)]^{1/2}} b^*_{k_1}b_{k+k_1}}_{③} \Big|. \end{aligned} \tag{A1}$$

In the above equation, it is evident that ① > ② and

$$\begin{aligned} ③ &< \sum_{k_1=k+p}^{\infty} \frac{\alpha}{\beta[kk_1|k-k_1|]^{1/2}} b^*_{k_1}b_{k+k_1} + \frac{\alpha}{\beta[k^2(k+k)]^{1/2}} b^*_k b_{2k} \\ &\sim \sum_{k_1=k+p}^{\infty} \frac{\alpha}{\beta[kk_1|k-k_1|]^{1/2}} b^*_{k_1}b_{k+k_1}. \end{aligned} \tag{A2}$$

Finally, we have

$$\text{Left-hand side} \sim \Big| \sum_{k_1=p,k_1\neq k}^{\infty} \frac{\alpha}{\beta[kk_1|k-k_1|]^{1/2}} b_{k_1}b_{k-k_1}\Big|. \tag{A3}$$

https://doi.org/10.1017/jfm.2026.11872 Published online by Cambridge University Press

Here, we note that if $b_k \sim O(1)$ for all k, the summation in (A3) (or (A1)) does not converge at the ∞ end, as can be seen by replacing the summation by an integral. This problem is avoided with assumption (i) by introducing a finite spectral bandwidth Δ. If one attempts to perform a more sophisticated analysis, the approach presented in Wu *et al.* (2025) can be followed.

In further evaluating (A3), it is critical to take into account the random phases in b_k (a procedure not considered in Zakharov (1999)). More precisely, with random phases in b_k the summation on the left-hand side behaves like a random walk in the complex plane, for which cancellations due to walks in different directions must be considered. For this reason, the summation on the left-hand side should be evaluated in terms of the expected value $E[|\sum \cdot|]$ or $\{E[|\sum \cdot|^2]\}^{1/2}$. Taking the latter expression, we have

$$\begin{aligned}\text{Left-hand side} &\sim \frac{\alpha}{\beta k^{1/2}}\left\{E\left[\left|\sum_{k_1=p,k_1\neq k}^{\infty}\frac{b_{k_1}b_{k-k_1}}{[k_1|k-k_1|]^{1/2}}\right|^2\right]\right\}^{1/2}\\ &\sim \frac{\alpha}{\beta k^{1/2}}\left\{\sum_{k_1=p,k_1\neq k}^{\infty}\frac{b_{k_1}b_{k_1}^{*}b_{k-k_1}b_{k-k_1}^{*}}{[k_1|k-k_1|]}\right\}^{1/2}\\ &\sim \frac{\alpha|b_k|^2}{\beta k^{3/2}}\sqrt{N_\Delta} \ll |b_k|,\end{aligned} \tag{A4}$$

where we have used Wick's pairing to obtain the second line, and assumptions (i) and (ii) to obtain the third line.

We now estimate b_k using (2.13) and (2.20), which yields

$$|b_k| \sim |\eta_k|/k^{1/2} \sim \frac{1}{\sqrt{N_\Delta}k^{1/2}}, \tag{A5}$$

where we have used $\sqrt{\sum_k |\eta_k|^2} \sim 1$ since the problem (e.g. significant wave height) has been scaled by a in (2.3).

Combining (A4) and (A5), we obtain $\alpha \ll \beta k^2$. If we further consider $k \sim 1$ (since the problem has been scaled by the peak wavenumber k_p), the condition is simply $\alpha \ll \beta$. Finally, we remark that the absence of N_Δ from the final result is only possible with the consideration of random phases in b_k.

Appendix B. Graphical proof regarding the resonant conditions

We consider the resonant condition

$$k_1 + k_2 = k_3 + k_4, \tag{B1}$$

$$\omega_1 + \omega_2 = \omega_3 + \omega_4, \tag{B2}$$

with a concave-down dispersion relation such as (2.9) and (2.8). For the sake of brevity, we will use the non-integrable Boussinesq equation with dispersion relation (2.9) as an example; however, the configurations generally hold for the full KB equation. A graphical illustration of the resonant conditions is shown in figures 10 and 11. Figure 10(a) represents the solution with all wavenumbers positive. However, in this case, this solution corresponds to the trivial solution of $k_1 = k_4$ and $k_2 = k_3$, which can be removed by a frequency renormalisation in the four-wave dynamical equation. Figure 10(b) corresponds to the solution with one wavenumber (say k_4) negative and the other three positive,

https://doi.org/10.1017/jfm.2026.11872 Published online by Cambridge University Press

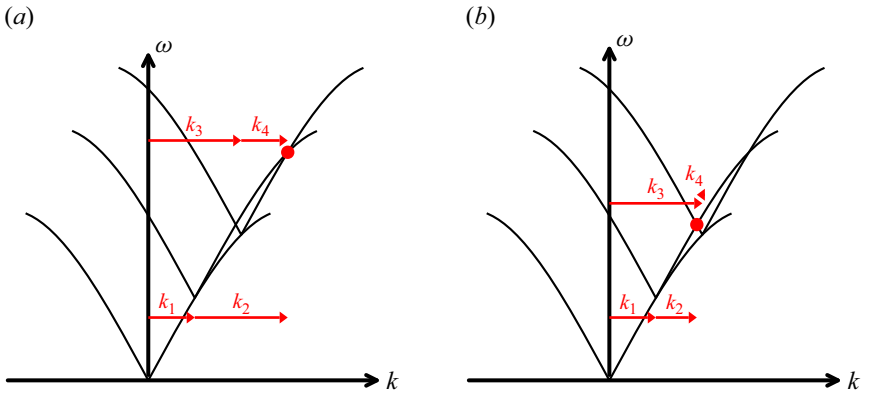


Figure 10. Graphical illustration of the resonant condition: (*a*) the case where all wavenumbers are positive; (*b*) the case where one wavenumber (say k_4) is negative and the others are positive.

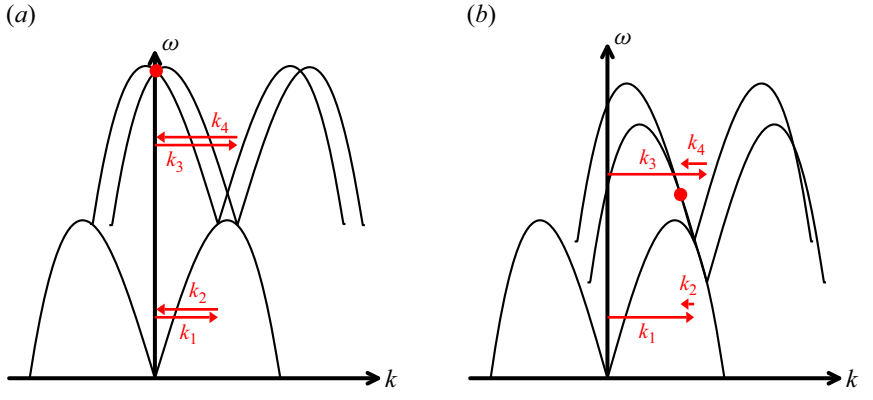


Figure 11. Graphical illustration of the spurious resonant conditions: (*a*) the case where all wavenumbers are $O(\beta^{-1/2})$; (*b*) the case where two wavenumbers are $O(1)$ and the other two are $O(\beta^{-1/2})$.

which persists in the WKE. Figures 11(*a*) and 11(*b*) correspond to configurations with two positive and two negative wavenumbers. Such configurations require either (i) $|k_1|, |k_2|, |k_3|, |k_4| = O(\beta^{-1/2})$, as shown in figure 11(*a*), or (ii) $|k_2|, |k_4| = O(1)$ and $|k_1|, |k_3| = O(\beta^{-1/2})$, as shown in figure 11(*b*). In either case, at least one of the $O(\beta^{-1/2})$ wavenumbers must lie on the descending branch of the dispersion relation, i.e. $|k| > k_*$ with $k_* = \sqrt{2/\beta}$ for (2.9) and $k^* = \sqrt{3/(2\beta)}$ for (2.8). However, it is in this region that both (2.9) and (2.8) deviate significantly from the shallow-water dispersion relation $\omega_k = |k|$, so these interactions are not physically relevant in the $\beta k^2 \ll 1$ regime of interest. We refer to these as spurious solutions and safely discard them in the theoretical and numerical analysis presented in this work. In all cases, we have used $k_{max} < k_*$, thus omitting the region in which this interaction is supported.

In summary, the only non-trivial, physically relevant solution for the resonant condition with a concave-down dispersion relation occurs when one wavenumber has an opposite sign to the other three.

https://doi.org/10.1017/jfm.2026.11872 Published online by Cambridge University Press

Appendix C. Calculation regarding T_I and T_{II}

The interaction coefficient (2.23) consists of twelve terms, of which three belong to T_I and nine to T_{II}, according to (2.26). We begin by evaluating T_I, illustrating the procedure with the first term in (2.26). Substituting (2.19) into (2.26) yields

$$\begin{aligned}-\frac{V_{k,3,k-3}V_{2,1,2-1}}{\omega_1+\omega_{2-1}-\omega_2} = &-\frac{\alpha^2(\omega_k\omega_3\omega_{k-3})^{1/2}(\omega_2\omega_1\omega_{2-1})^{1/2}}{32(\omega_1+\omega_{2-1}-\omega_2)}\\ &\times[W_{k,3}+W_{k,k-3}+W_{3,k-3}]\\ &\times[W_{2,1}+W_{2,2-1}+W_{1,2-1}],\end{aligned} \tag{C1}$$

where $W_{i,j}=W(i,\,j)$. We consider the condition corresponding to configuration 1, where k, k_1, k_2 are positive and k_3 is negative, with $\kappa_2>\kappa$, κ_1, κ_3. The denominator of (C1) can be expanded using (2.9), yielding

$$\omega_1+\omega_{2-1}-\omega_2=\frac{1}{2}\beta\kappa\kappa_1\kappa_2(\kappa_2-\kappa_1), \tag{C2}$$

where the linear contribution from each term cancels and only $O(\beta)$ terms remain. Substituting this expression into (C1), and keeping only terms at leading order, gives

$$-\frac{V_{k,3,k-3}V_{2,1,2-1}}{\omega_1+\omega_{2-1}-\omega_2}=\frac{3\alpha^2}{16\beta}\left(\frac{\kappa_3\kappa}{\kappa_1\kappa_2}\right)^{1/2}. \tag{C3}$$

Implementing the same procedure for the remaining T_I terms, we obtain

$$-\frac{V_{1,3,1-3}V_{2,k,2-k}}{\omega_k+\omega_{2-k}-\omega_2}=\frac{3\alpha^2}{16\beta}\left(\frac{\kappa_1\kappa_3}{\kappa\kappa_2}\right)^{1/2} \tag{C4}$$

and

$$-\frac{V_{k+1,k,1}V_{2+3,2,3}}{\omega_{k+1}-\omega_k-\omega_1}=-\frac{3\alpha^2}{16\beta}\left(\frac{\kappa_3\kappa_2}{\kappa\kappa_1}\right)^{1/2}. \tag{C5}$$

By grouping (C3)–(C5) and using $\kappa_3=\kappa_2-\kappa-\kappa_1$, we can obtain a compact expression for T_I:

$$T_I=-\frac{3\alpha^2}{16\beta}\left(\frac{\kappa_3^3}{\kappa\kappa_1\kappa_2}\right)^{1/2}. \tag{C6}$$

We next evaluate the contribution from the T_{II} terms in (2.26). The terms in T_{II} can be further subdivided into T_{II}^a and T_{II}^b based on how the linear terms in the denominator cancel – those with two linear terms after cancellation grouped into T_{II}^a and those with one linear term grouped into T_{II}^b. Under this classification, T_{II}^a includes the first, third and eleventh term in (2.23), and T_{II}^b includes the remaining terms. We begin with an example of the calculation of one term in T_{II}^a, specifically taking the first term in (2.23):

$$\begin{aligned}-\frac{V_{k,2,k-2}V_{3,1,3-1}}{\omega_2+\omega_{k-2}-\omega_k} = &-\frac{\alpha^2(\omega_k\omega_2\omega_{k-2})^{1/2}(\omega_3\omega_1\omega_{3-1})^{1/2}}{32(\omega_2+\omega_{k-2}-\omega_k)}\\ &\times[W_{k,2}+W_{k,k-2}+W_{2,k-2}][W_{3,1}+W_{3,3-1}+W_{1,3-1}].\end{aligned} \tag{C7}$$

https://doi.org/10.1017/jfm.2026.11872 Published online by Cambridge University Press

Expanding the denominator and using $\omega_{\kappa-2} = (\kappa_2 - \kappa) - \beta/6(\kappa_2 - \kappa)^3$ (due to configuration 1) gives

$$\omega_2 + \omega_{k-2} - \omega_k = -2(\kappa_2 - \kappa) - \frac{\beta}{6}\left[\kappa_2^3 + (\kappa_2 - \kappa)^3 - \kappa^3\right]. \tag{C8}$$

Substituting the expression above and only keeping terms at leading order into (C7) yields

$$-\frac{V_{k,2,k-2}V_{3,1,3-1}}{\omega_2 + \omega_{k-2} - \omega_k} = -\frac{\alpha^2}{64}(\kappa\kappa_1\kappa_2\kappa_3)^{1/2}, \tag{C9}$$

where the result is only one term after some cancellations. By repeating the same procedure for the remaining two T_{II}^a terms, one obtains

$$-\frac{V_{1,2,1-2}V_{3,k,3-k}}{\omega_2 + \omega_{1-2} - \omega_1} = -\frac{\alpha^2}{64}(\kappa\kappa_1\kappa_2\kappa_3)^{1/2} \tag{C10}$$

and

$$-\frac{V_{-k-1,k,1}V_{-2-3,2,3}}{\omega_{k+1} + \omega_k + \omega_1} = -\frac{\alpha^2}{64}(\kappa\kappa_1\kappa_2\kappa_3)^{1/2}. \tag{C11}$$

We next move onto terms belonging to T_{II}^b, using the second term in (2.23) as an example:

$$-\frac{V_{k,2,k-2}V_{3,1,3-1}}{\omega_1 + \omega_{3-1} - \omega_3} = -\frac{\alpha^2(\omega_k\omega_2\omega_{k-2})^{1/2}(\omega_3\omega_1\omega_{3-1})^{1/2}}{32(\omega_1 + \omega_{3-1} - \omega_3)} \times [W_{k,2} + W_{k,k-2} + W_{2,k-2}][W_{3,1} + W_{3,3-1} + W_{1,3-1}]. \tag{C12}$$

Expanding the denominator and using $\omega_{3-1} = (\kappa_3 + \kappa_1) - \beta/6(\kappa_3 + \kappa_1)^2$ (recall configuration 1) reveals that only one linear term remains:

$$\omega_1 + \omega_{3-1} - \omega_3 = 2\kappa_1 - \frac{\beta}{6}\left[\kappa_1^3 + (\kappa_3 + \kappa_1)^3 - \kappa_3^3\right]. \tag{C13}$$

Substituting the above expression into (C12) and retaining only the leading-order contribution gives

$$-\frac{V_{k,2,k-2}V_{3,1,3-1}}{\omega_1 + \omega_{3-1} - \omega_3} = -\frac{\alpha^2\kappa_3(\kappa\kappa_1\kappa_2\kappa_3)^{1/2}}{64\kappa_1} - \frac{\alpha^2}{64}(\kappa\kappa_1\kappa_2\kappa_3)^{1/2}. \tag{C14}$$

Carrying out the same calculation for the five remaining T_{II}^b gives

$$-\frac{V_{1,2,1-2}V_{3,k,3-k}}{\omega_k + \omega_{3-k} - \omega_3} = -\frac{\alpha^2\kappa_3(\kappa\kappa_1\kappa_2\kappa_3)^{1/2}}{64\kappa} - \frac{\alpha^2}{64}(\kappa\kappa_1\kappa_2\kappa_3)^{1/2}, \tag{C15}$$

$$-\frac{V_{k,3,k-3}V_{2,1,2-1}}{\omega_3 + \omega_{k-3} - \omega_k} = \frac{3\alpha^2\kappa(\kappa\kappa_1\kappa_2\kappa_3)^{1/2}}{64\kappa_3} + \frac{3\alpha^2}{64}(\kappa\kappa_1\kappa_2\kappa_3)^{1/2}, \tag{C16}$$

$$-\frac{V_{1,3,1-3}V_{2,k,2-k}}{\omega_3 + \omega_{1-3} - \omega_1} = \frac{3\alpha^2\kappa_1(\kappa\kappa_1\kappa_2\kappa_3)^{1/2}}{64\kappa_3} + \frac{3\alpha^2}{64}(\kappa\kappa_1\kappa_2\kappa_3)^{1/2}, \tag{C17}$$

$$-\frac{V_{k+1,k,1}V_{2+3,2,3}}{\omega_{2+3} - \omega_2 - \omega_3} = \frac{3\alpha^2}{64}(\kappa\kappa_1\kappa_2\kappa_3)^{1/2} - \frac{3\alpha^2\kappa_2(\kappa\kappa_1\kappa_2\kappa_3)^{1/2}}{64\kappa_3} \tag{C18}$$

and

$$-\frac{V_{-k-1,k,1}V_{-2-3,2,3}}{\omega_{2+3} + \omega_2 + \omega_3} = \frac{\alpha^2\kappa_3(\kappa\kappa_1\kappa_2\kappa_3)^{1/2}}{64\kappa_2} - \frac{\alpha^2}{64}(\kappa\kappa_1\kappa_2\kappa_3)^{1/2}. \tag{C19}$$

https://doi.org/10.1017/jfm.2026.11872 Published online by Cambridge University Press

Grouping terms (C9)–(C11) for T_{II}^{a} and (C14)–(C19) for T_{II}^{b} and using the relation $\kappa_3 = \kappa_2 - \kappa - \kappa_1$ yields

$$T_{II}^{a} = -\frac{3\alpha^2}{64}(\kappa\kappa_1\kappa_2\kappa_3)^{1/2},$$
$$T_{II}^{b} = \frac{\alpha^2}{64}(\kappa\kappa_1\kappa_2\kappa_3)^{1/2}\left[3 - \kappa_3\left(\frac{1}{\kappa_1} - \frac{1}{\kappa_2} + \frac{1}{\kappa}\right)\right]. \tag{C20}$$

Combining T_{II}^{a} and T_{II}^{b} yields the compact expression

$$T_{II} = -\frac{\alpha^2}{64}(\kappa\kappa_1\kappa_2\kappa_3)^{1/2}\left[\kappa_3\left(\frac{1}{\kappa_1} - \frac{1}{\kappa_2} + \frac{1}{\kappa}\right)\right]. \tag{C21}$$

Equations (C6) and (C21) are given by (2.27*a*,*b*) in § 2.1 of the main paper.

Appendix D. Details of KZ spectra derivation

D.1. *Reduction of resonance condition in I terms*

We begin by using I_1 as an example. To impose the resonant constraint, we substitute the wavenumber resonance condition $\kappa_3 = -\kappa - \kappa_1 + \kappa_2$ into the frequency resonance condition using (2.9), which gives

$$\omega_\kappa + \omega_1 - \omega_2 - \omega_3 = -2\kappa_3 - \frac{\beta}{6}\left(\kappa^3 + \kappa_1^3 - \kappa_2^3 - \kappa_3^3\right) = 0. \tag{D1}$$

For a non-trivial solution, κ_3 must be of $O(\beta)$. As a result, $k_3^3 = O(\beta^3)$ is negligible at leading order and can be omitted, yielding

$$\kappa_3 = \frac{\beta}{12}\left(\kappa_2^3 - \kappa^3 - \kappa_1^3\right). \tag{D2}$$

The argument of the wavenumber delta function may be written as

$$\kappa + \kappa_1 - \kappa_2 + O(\beta) = 0, \tag{D3}$$

since it is appropriate to neglect the $O(\beta)$ term at leading order. This new resonant condition implies $\kappa_2 = \kappa + \kappa_1$, which simplifies (D2) to

$$\kappa_3 = \frac{\beta}{4}\kappa\kappa_1\kappa_2. \tag{D4}$$

Following a similar procedure, we obtain the relations $\kappa_2 = (\beta/4)\kappa\kappa_1\kappa_3$ and $\kappa_1 = (\beta/4)\kappa\kappa_2\kappa_3$ corresponding to I_2 and I_3, respectively. Substituting these $\kappa_i \sim \beta$ terms into the interaction coefficient (2.30) and integrating out the frequency condition in each case yields (2.33)–(2.35) presented in the main paper.

D.2. *Case A*

We seek stationary power-law solutions of the form $n_\kappa \sim \kappa^{-x}$. The total interaction is given by (2.40) in the main paper, with the kernel R_{12}^{κ} defined by (2.39). We adopt the reference form $R_{12}^{\kappa} \propto (\kappa\kappa_1\kappa_2)^{2-x}\delta(\kappa - \kappa_2 - \kappa_1)$ and rewrite the other two permutations, $R_{1\kappa}^{2}$ and $R_{\kappa 2}^{1}$, into this form via Zakharov transformations as introduced in Zakharov *et al.* (2012). Inserting the power-law solution ansatz and performing the Zakharov transformation on $R_{1\kappa}^{2}$ using $\kappa_1 = \kappa^2/\tilde{\kappa}_1$ and $\kappa_2 = \kappa\tilde{\kappa}_2/\tilde{\kappa}_1$ with Jacobian $|\kappa^3/\tilde{\kappa}_1^3|$ yields

https://doi.org/10.1017/jfm.2026.11872 Published online by Cambridge University Press

$$R^2_{1\kappa}\mathrm{d}\kappa_1\mathrm{d}\kappa_2 \propto \left(\kappa^{10-4x}\tilde{\kappa}_1^{2x-6}\tilde{\kappa}_2^{2-x}\right)\delta(\kappa-\tilde{\kappa}_2-\tilde{\kappa_1})\mathrm{d}\tilde{\kappa_1}\mathrm{d}\tilde{\kappa_2}. \tag{D5}$$

From this, the integral contribution relative to the reference kernel becomes

$$I_2 = \int \left(\frac{\kappa_1}{\kappa}\right)^{3x-8} R^{\kappa}_{12}\,\mathrm{d}\kappa_1\,\mathrm{d}\kappa_2, \tag{D6}$$

which serves as a key component for determining the stationary scaling exponent.

Following the same procedure for $R^1_{\kappa 2}$ with $\kappa_1 = \kappa\tilde{\kappa}_1/\tilde{\kappa_2}$, $\kappa_2 = \kappa^2/\tilde{\kappa}_2$ and Jacobian $|\kappa^3/\tilde{\kappa}_2^3|$ yields

$$R^1_{\kappa 2}\mathrm{d}\kappa_1\mathrm{d}\kappa_2 \propto \left(\kappa^{10-4x}\tilde{\kappa}_1^{2-x}\tilde{\kappa}_2^{2x-6}\right)\delta(\kappa-\tilde{\kappa}_2-\tilde{\kappa_1})\mathrm{d}\tilde{\kappa_1}\mathrm{d}\tilde{\kappa_2}, \tag{D7}$$

which in turn yield

$$I_3 = \int \left(\frac{\kappa_2}{\kappa}\right)^{3x-8} R^{\kappa}_{12}\,\mathrm{d}\kappa_1\,\mathrm{d}\kappa_2. \tag{D8}$$

The total contribution can then be written as

$$I = \int R^{\kappa}_{12}\left[1-\left(\frac{\kappa_1}{\kappa}\right)^{3x-8}-\left(\frac{\kappa_2}{\kappa}\right)^{3x-8}\right]\mathrm{d}\kappa_1\,\mathrm{d}\kappa_2, \tag{D9}$$

which is presented as (2.41) in the main paper.

D.3. *Case B*

Here we consider the solution ansatz $n_\kappa \sim \kappa^{-x}$ and take $R^{\kappa}_{12} \propto \kappa^{2-2x}\kappa_1^{2-2x}\kappa_2^{2-2x}$ (from (2.46) in the main paper) as the reference form. Applying the same Zakharov transformation outlined in Appendix D.2 to $R^2_{1\kappa}$ yields

$$R^2_{1\kappa}\mathrm{d}\kappa_1\mathrm{d}\kappa_2 = 4^x\beta^{-x}\left(\kappa^{10-8x}\tilde{\kappa}_1^{4x-6}\tilde{\kappa}_2^{2-2x}\right)\delta(\kappa-\tilde{\kappa}_2-\tilde{\kappa}_1)\mathrm{d}\tilde{\kappa_1}\mathrm{d}\tilde{\kappa_2}. \tag{D10}$$

Consequently, the integral contribution relative to the reference kernel is

$$I_2 = \int \left(\frac{\kappa_1}{\kappa}\right)^{6x-8} R^{\kappa}_{12}\,\mathrm{d}\kappa_1\,\mathrm{d}\kappa_2. \tag{D11}$$

Applying the same procedure to $R^1_{\kappa 2}$ using the transformations outlined in Appendix D.2 gives the following:

$$R^1_{\kappa 2}\mathrm{d}\kappa_1\mathrm{d}\kappa_2 = 4^x\beta^{-x}\left(\kappa^{10-8x}\tilde{\kappa}_1^{2-2x}\tilde{\kappa}_2^{4x-6}\right)\delta(\kappa-\tilde{\kappa}_2-\tilde{\kappa}_1)\mathrm{d}\tilde{\kappa_1}\mathrm{d}\tilde{\kappa_2}, \tag{D12}$$

which yields

$$I_3 = \left(\frac{\kappa_2}{\kappa}\right)^{6x-8} R^{\kappa}_{12}\,\mathrm{d}\kappa_1\,\mathrm{d}\kappa_2. \tag{D13}$$

The total interaction term can therefore be written as

$$I = \int R^{\kappa}_{12}\left[1-\left(\frac{\kappa_1}{\kappa}\right)^{6x-8}-\left(\frac{\kappa_2}{\kappa}\right)^{6x-8}\right]\mathrm{d}\kappa_1\,\mathrm{d}\kappa_2, \tag{D14}$$

which corresponds to (2.47) in the main paper.

D.4. *Locality of solutions*

We analyse the locality of the spectrum $n_\kappa \sim \kappa^{-x}$ by evaluating the behaviour in the infrared (IR) and ultraviolet (UV) limits.

https://doi.org/10.1017/jfm.2026.11872 Published online by Cambridge University Press

We begin by assessing the behaviour in the IR limit for Case A. To this end, we take $\kappa_1 \to 0$. Expressing the interaction term R^{κ}_{12} given by (2.39) in terms of the power-law ansatz yields

$$R^{\kappa}_{12} \propto (\kappa\kappa_1\kappa_2)^2\left(\kappa^{-x}\kappa_1^{-x}\kappa_2^{-x}\right)\delta(\kappa-\kappa_2-\kappa_1). \tag{D15}$$

Integrating out κ_2 we obtain

$$R^a(\kappa,\kappa_1) \propto \kappa^{2-x}\kappa_1^{2-x}(\kappa-\kappa_1)^{2-x}. \tag{D16}$$

Expanding the $(\kappa-\kappa_1)^{2-x}$ term in (D16) leads to

$$(\kappa-\kappa_1)^{2-x} \approx \kappa^{2-x} - (2-x)\kappa^{1-x}\kappa_1 + \cdots, \tag{D17}$$

which can then be substituted back into (D16), yielding

$$R^a(\kappa,\kappa_1) \propto \kappa_1^{2-x}\kappa^{4-2x} - (2-x)\kappa^{3-2x}\kappa_1^{3-x}. \tag{D18}$$

Following the same procedure for $R^2_{1\kappa}$, we obtain

$$R^b(\kappa,\kappa_1) \propto \kappa_1^{2-x}\kappa^{4-2x} + (2-x)\kappa^{3-2x}\kappa_1^{3-x}. \tag{D19}$$

In the case of $R^1_{\kappa_2}$, taking $\kappa_1 \to 0$ while κ as $O(1)$ means that the resonance condition cannot be satisfied, therefore $R^c(\kappa,\kappa_1)=0$. From the total interaction integral

$$I(\kappa) = \int \left(R^a - R^b - R^c\right)\mathrm{d}\kappa_1 \sim \int \kappa_1^{3-x}\,\mathrm{d}\kappa_1, \tag{D20}$$

where we see that (D18) and (D19) cancel at the leading order. For the integral (D20) to converge, we require $3-x>-1$, resulting in the condition

$$\text{IR convergence (A):} \quad x<4. \tag{D21}$$

Next, we assess the behaviour in the UV limit for Case A by taking $\kappa_1 \to \infty$. For R^{κ}_{12}, the resonance condition cannot be satisfied when taking $\kappa_1 \to \infty$, thus it does not contribute (i.e. $R^a(\kappa,\kappa_1)=0$). For the next term with the solution ansatz

$$R^2_{1\kappa} \propto (\kappa\kappa_1\kappa_2)^2\left(\kappa^{-x}\kappa_1^{-x}\kappa_2^{-x}\right)\delta(\kappa_2-\kappa-\kappa_1). \tag{D22}$$

Integrating out κ_2 yields

$$R^b(\kappa,\kappa_1) \propto \kappa^{2-x}\kappa_1^{2-x}(\kappa_1+\kappa)^{2-x}, \tag{D23}$$

which, upon substitution of the expansion $(\kappa_1+\kappa)^{2-x} \approx \kappa_1^{2-x} + (2-x)\kappa_1^{1-x}\kappa + \cdots$, yields

$$R^b(\kappa,\kappa_1) \propto \kappa^{2-x}\kappa_1^{4-2x} - (2-x)\kappa^{3-x}\kappa_1^{3-2x}. \tag{D24}$$

Following the same procedure for $R^1_{\kappa 2}$ gives

$$R^c(\kappa,\kappa_1) \propto \kappa^{2-x}\kappa_1^{4-2x} + (2-x)\kappa^{3-x}\kappa_1^{3-2x}. \tag{D25}$$

Explicitly evaluating $R^a - R^b - R^c$ reveals the following scaling in the UV limit:

$$I(\kappa) \sim \int \kappa_1^{4-2x}\,\mathrm{d}\kappa_1. \tag{D26}$$

Convergence of (D26) therefore requires $4-2x<-1$, yielding the criterion

$$\text{UV convergence (A):} \quad x>5/2. \tag{D27}$$

https://doi.org/10.1017/jfm.2026.11872 Published online by Cambridge University Press

We next assess the behaviour in the IR limit for Case B by making $\kappa_1 \to 0$. If we express (2.46) in terms of the power-law ansatz $n_\kappa \sim \kappa^{-x}$, we obtain

$$R^{\kappa}_{12} \propto (\kappa\kappa_1\kappa_2)^2\left(\kappa^{-x}\kappa_1^{-x}\kappa_2^{-x}\kappa_3^{-x}\right)\left(\kappa^x - \kappa_1^x - \kappa_2^x\right)\delta(\kappa - \kappa_2 - \kappa_1). \tag{D28}$$

Using $\kappa_3 = (\beta/4)\kappa_1\kappa_2\kappa_2$ from (D4), we can simplify (D28) to

$$R^{\kappa}_{12} \propto (\kappa\kappa_1\kappa_2)^{2-2x}\left(\kappa^x - \kappa_1^x - \kappa_2^x\right)\delta(\kappa - \kappa_1 - \kappa_2). \tag{D29}$$

Integrating out κ_2 gives

$$R^a(\kappa, \kappa_1) \propto (\kappa\kappa_1(\kappa - \kappa_1))^{2-2x}\left(\kappa^x + \kappa_1^x - (\kappa - \kappa_1)^x\right), \tag{D30}$$

which upon substituting the expansion of $(\kappa - \kappa_1)^x$ and $(\kappa - \kappa_1)^{2-2x}$ yields

$$R^a(\kappa, \kappa_1) \propto x\kappa^{3-3x}\kappa_1^{3-2x} - (2 - 2x)x\kappa^{2-3x}\kappa_1^{4-2x}. \tag{D31}$$

Following the same procedure for $R^2_{1\kappa}$ gives

$$R^b(\kappa, \kappa_1) \propto x\kappa^{3-3x}\kappa_1^{3-2x} + (2 - 2x)x\kappa^{2-3x}\kappa_1^{4-2x}. \tag{D32}$$

As stated in Case A, $R^1_{\kappa 2}$ does not contribute when $\kappa_1 \to 0$, therefore $R^c(\kappa, \kappa_1) = 0$. Explicitly evaluating $R^a - R^b - R^c$ shows that the leading-order terms of (D31) and (D32) cancel. Thus, the integral in the IR limit behaves like

$$I(\kappa) \sim \int \kappa_1^{4-2x}\, \mathrm{d}\kappa_1. \tag{D33}$$

For (D33) to converge, the exponent must satisfy $4 - 2x > -1$, which yields the condition

$$\text{IR convergence (B):} \quad x < 5/2. \tag{D34}$$

Next, we take $\kappa_1 \to \infty$ to assess behaviour in the UV limit. In this scenario, $R^{\kappa}_{12} = 0$ (and thus $R^a(\kappa, \kappa_1) = 0$) for the same reason stated above for Case A. The interaction term $R^2_{1\kappa}$ can be expressed as

$$R^2_{1\kappa} \propto (\kappa\kappa_1\kappa_2)^{2-2x}\left(\kappa_2^x - \kappa^x - \kappa_1^x\right)\delta(\kappa_2 - \kappa - \kappa_1). \tag{D35}$$

After integrating out κ_2 we get

$$R^b(\kappa, \kappa_1) \propto (\kappa\kappa_1(\kappa_1 + \kappa))^{2-2x}\left(\kappa^x + \kappa_1^x - (\kappa_1 + \kappa)^x\right), \tag{D36}$$

into which we substitute the expansion for $(\kappa_1 + \kappa)^{2-2x}$ and $(\kappa_1 + \kappa)^x$ yielding

$$R^b(\kappa, \kappa_1) \propto \left(2x - 2x^2\right)\kappa^{4-2x}\kappa_1^{3-2x} + x\kappa^{3-2x}\kappa_1^{3-3x}. \tag{D37}$$

Carrying out the same procedure on $R^1_{2\kappa}$ gives

$$R^c(\kappa, \kappa_1) \propto -\left(2x - 2x^2\right)\kappa^{4-2x}\kappa_1^{3-2x} + x\kappa^{3-2x}\kappa_1^{3-3x}. \tag{D38}$$

Evaluating $R^a - R^b - R^c$ shows that the first terms in (D37) and (D38) cancel, and the integral scales as

$$I(\kappa) \sim \int \kappa_1^{3-3x}\, \mathrm{d}\kappa_1. \tag{D39}$$

In order for the integral to converge, we require $3 - 3x < -1$, leading to the condition

$$\text{UV convergence (B):} \quad x > 4/3. \tag{D40}$$

https://doi.org/10.1017/jfm.2026.11872 Published online by Cambridge University Press

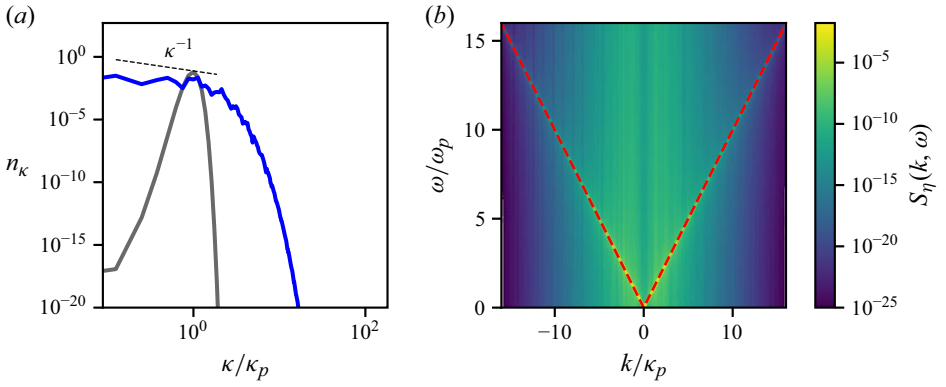


Figure 12. (*a*) The initial (solid grey) and stationary (solid blue) spectra at $t = 0$ and $t \approx 4 \times 10^5 T_p$ for the free-evolution case with $\alpha = \beta = 4 \times 10^{-5}$. The RJ scaling is marked (dashed black line). (*b*) The k–ω spectrum corresponding to the wavenumber range following the RJ scaling. The KB dispersion relation (2.8) is indicated by the dashed red line.

Appendix E. Free-evolution case for initial spectrum peaked at low k

In this appendix, we examine a free-evolution case with an extended wavenumber range and a spectral peak located at larger scales. We set $\alpha = \beta = 4 \times 10^{-5}$, ensuring that $(\beta/3)\kappa_{max}^2 \ll 1$. Figure 12(*a*) shows that the RJ-like scaling of $n_\kappa \sim \kappa^{-1}$ is observed to the left of the spectral peak; however, we do not see this scaling propagate towards smaller scales. This is likely due to three-wave quasi-resonant interactions preferentially transferring energy towards large scales (e.g. interactions where two large wavenumbers generate a small wavenumber). We therefore do not interpret the RJ-type scaling observed here in the classical wave turbulence sense, as such spectra are expected to exhibit universality across the entire wavenumber range, without abrupt exponential tails. Figure 12(*b*) presents the wavenumber–frequency spectrum for the wavenumber range exhibiting RJ-like scaling to confirm that we are operating in the weakly nonlinear regime, without the presence of solitons.

Appendix F. Unidirectional KdV simulations

Following the procedure outlined in Karczewska & Rozmej (2018) (see Ch. 3), a KdV equation can be derived from the KB system (2.4) and (2.5) by eliminating one direction of wave propagation. The KdV equation reads

$$\eta_t + \eta_x + \frac{3}{2}\alpha\eta\eta_x + \frac{1}{6}\beta\eta_{xxx} = 0. \tag{F1}$$

We perform numerical simulations of (F1) using a pseudospectral method combined with an IF-RK4 time-marching scheme. The computational set-up follows the configuration detailed in § 3.1.1, with the sole modification that the initial condition now only contains right-propagating waves. Figure 13(*a*) compares the spectral evolution of the KdV equation and the KB system for $\alpha = \beta = 0.2$. Both spectra reach the same RJ form on the same time scale, with the respective spectra evaluated at $t = 5 \times 10^5 T_p$. This behaviour is to be expected, as when nonlinearity and dispersion are balanced, the dynamics is primarily governed by quasi-resonant triad interactions, which are supported in both KB and KdV frameworks.

https://doi.org/10.1017/jfm.2026.11872 Published online by Cambridge University Press

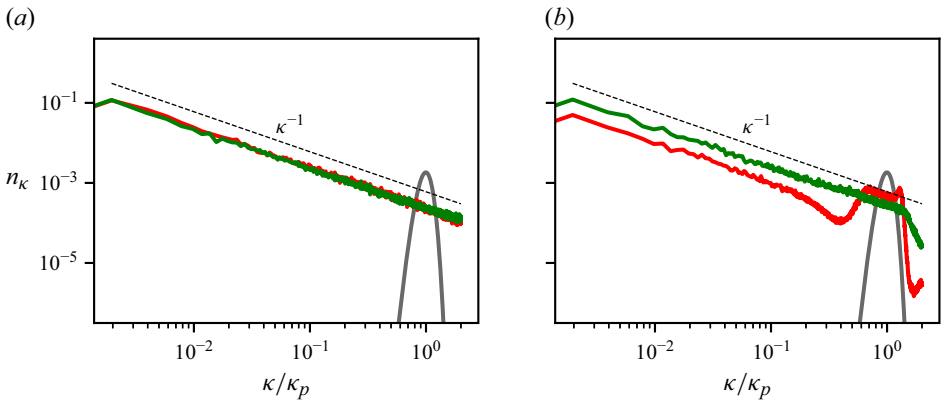


Figure 13. The spectrum $n_k \propto |\eta_k|^2/\omega_k$ at the initial (solid grey) and stationary state for KB (solid green) and KdV (red) for (*a*) $\alpha = 0.2$ taken at $5 \times 10^5 T_p$ and (*b*) $\alpha = 0.02$ taken at $1.2 \times 10^6 T_p$. The RJ scaling is marked (dashed black).

In contrast, figure 13(*b*) presents the spectral evolution for $\alpha = 0.02$ in the regime $\alpha \ll \beta$, where a clear disparity emerges between the dynamics of the KdV equation and the KB system. We see that the spectrum from the KB equation develops a state consistent with RJ scaling at all scales, whereas the spectrum of the KdV equation only exhibits this behaviour at large scales. We recall that in this regime of $\alpha \ll \beta$, the normal-form transformation is valid and the quasi-resonant quartet interactions may begin to play a significant role in the spectral evolution. This is indeed the mechanism driving the development of the RJ scaling in the KB spectrum towards moderate-to-small scales, which, on the other hand, is absent in the KdV system. We further note that the validity condition of the normal-form transformation requires the spectrum to decay sufficiently fast at large scales, which is not the case in the simulations (more precisely, the validity condition should read $\alpha \ll \beta k^2$, which is not satisfied at small k). Therefore, the evolution of large scales may still be driven by triad quasi-resonances in both the KB and KdV simulations, as we observe in figure 13(*b*).

Appendix G. Numerical scheme and validation

G.1. *Time integration scheme*

In this appendix, we describe the IF-RK4 scheme for the KB system. We start by splitting the linear and nonlinear parts of equations (2.4) and (2.5) and expressing them in Fourier space (essentially following the procedure in Pan (2020)):

$$\frac{\partial}{\partial t}\begin{bmatrix}\hat{\eta}_k \\ \hat{u}_k\end{bmatrix} = ik\begin{bmatrix}0 & -1+\dfrac{\beta}{3}k^2 \\ -1 & 0\end{bmatrix}\begin{bmatrix}\hat{\eta}_k \\ \hat{u}_k\end{bmatrix} + \begin{bmatrix}\hat{P}_k \\ \hat{Q}_k\end{bmatrix}, \tag{G1}$$

where $\hat{\eta}_k$ and $\hat{u}_k$ are the Fourier transforms of $\eta(x)$ and $u(x)$, and $\hat{P}_k$ and $\hat{Q}_k$ represent the nonlinear terms in (2.4) and (2.5). Diagonalising (G1) yields

$$\frac{\partial}{\partial t}\begin{bmatrix}v_1 \\ v_2\end{bmatrix} = ik\begin{bmatrix}\lambda_1 & 0 \\ 0 & \lambda_2\end{bmatrix}\begin{bmatrix}v_1 \\ v_2\end{bmatrix} + \begin{bmatrix}F_1 \\ F_2\end{bmatrix}, \tag{G2}$$

https://doi.org/10.1017/jfm.2026.11872 Published online by Cambridge University Press

where $\lambda_1 = -ik\sqrt{1-(\beta/3)k^2}$ and $\lambda_2 = ik\sqrt{1-(\beta/3)k^2}$, and

$$\begin{bmatrix} v_1 \\ v_2 \end{bmatrix} = \Omega^{-1} \begin{bmatrix} \hat{\eta}_k \\ \hat{u}_k \end{bmatrix}, \tag{G3}$$

$$\begin{bmatrix} F_1 \\ F_2 \end{bmatrix} = \Omega^{-1} \begin{bmatrix} \hat{P}_k \\ \hat{Q}_k \end{bmatrix}, \tag{G4}$$

with

$$\Omega = \begin{bmatrix} \sqrt{1-\frac{\beta}{3}k^2} & -\sqrt{1-\frac{\beta}{3}k^2} \\ 1 & 1 \end{bmatrix}. \tag{G5}$$

We then define $\Psi_1 = \exp(-\lambda_1 t)v_1$ and $\Psi_2 = \exp(-\lambda_2 t)v_2$, with which (G2) can be transformed into

$$\frac{\partial}{\partial t}\Psi_1 = \exp(-\lambda_1 t)F_1, \tag{G6}$$

$$\frac{\partial}{\partial t}\Psi_2 = \exp(-\lambda_2 t)F_2. \tag{G7}$$

Equations (G6) and (G7) can then be integrated using the standard RK4 scheme. In each simulation, we select a fixed time step for each parameter set. Since the integrating factor mitigates the linear stiffness, the time step is chosen to ensure the nonlinear term is adequately resolved. The choice of time step is validated by monitoring the conservation of energy and momentum in the absence of forcing and dissipation. This combined IF-RK4 scheme essentially solves the linear part of (G2) analytically (to machine precision; see figure 14 for validation). For the non-integrable Boussinesq variant, we modify the linear operator in (G1) to yield $\omega_k = k(1-(\beta/6)k^2)$, with eigenvalues $\lambda_1 = -i\omega_k$ and $\lambda_2 = i\omega_k$. The diagonalisation and IF-RK4 update are then applied exactly as above. A similar scheme is implemented for simulations of the KdV equation. An integrating factor can be applied directly to the KdV equation (Trefethen 2000), in contrast to the coupled KB system which must first be diagonalised.

For both KB and KdV, the spatial derivatives, including the nonlinear terms $\hat{P}_k$ and $\hat{Q}_k$ in the former, are computed using fast Fourier transforms. To mitigate aliasing errors, we use a 1/2 de-aliasing rule.

G.2. *Validation of the KB system*

We perform a series of tests to validate the aforementioned methods. We begin by ensuring that the linear part of the KB system is solved to machine precision using the integrating factor scheme. To do this, we set $\alpha = 0$, and discarding the nonlinear terms in (2.4) and (2.5), we are left with

$$\eta_t = -u_x - \frac{1}{3}\beta u_{xxx}, \tag{G8}$$

$$u_t = -\eta_x. \tag{G9}$$

https://doi.org/10.1017/jfm.2026.11872 Published online by Cambridge University Press

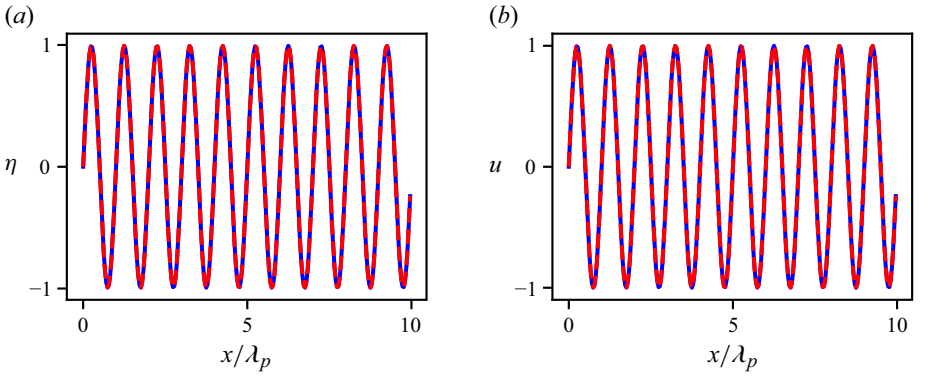


Figure 14. Comparison of the numerical (solid blue) and analytical (dashed red) solutions for (*a*) surface elevation and (*b*) velocity for the linear portion of the KB system at $t = 10T_p$.

This system has an exact solution of the form $\sin(kx - \omega t)$. Substituting this in for u, we get

$$\begin{aligned} u(x,t) &= \sin(kx - \omega t), \\ \eta(x,t) &= \frac{\omega}{k}\sin(kx - \omega t), \end{aligned} \tag{G10}$$

where the dispersion relation is given by (2.8). For this test case, we set $\beta = 1$ and use (G10) as our initial condition with $t = 0$. Figure 14 shows the numerical solution compared against the analytic solution after $10T_p$. Both the velocity component and the surface elevation are within machine precision of the analytic solution.

We proceed with the full KB system where we set $\alpha = \beta = 1$. The solver is tested using a known exact soliton solution (example taken from Juliussen (2014)):

$$\begin{aligned} u(x,t) &= \frac{2(c^2-1)}{\cosh(\sqrt{3(c^2-1)}(x - ct)) + c}, \\ \eta(x,t) &= cu(x,t) - \frac{1}{2}u^2(x,t), \end{aligned} \tag{G11}$$

with $c = 1.005$. We characterise the time scale of the system by the pulse duration $\tau_s = \mathrm{FWHM}/c$ where FWHM is the full width at half-maximum for the soliton profile and c is the soliton velocity. We allow the soliton to propagate for $2\tau_s$. Figure 15 shows a comparison between the numerical and analytical solutions at $2\tau_s$, demonstrating the high accuracy of the numerical results. We test the conservation of two quantities, the total energy H and the total momentum P, defined by the integrals

$$H(t) = \int E(x,t)\,\mathrm{d}x, \qquad P(t) = \int I(x,t)\,\mathrm{d}x. \tag{G12}$$

For the KB system, the energy density E is expressed as

$$E = \frac{\alpha^2}{2}\eta^2 + \frac{\alpha^2}{2}(1 + \alpha\eta)u^2 + \frac{\alpha^2\beta}{3}uu_{xx} + \frac{\alpha^2\beta}{6}u_x^2, \tag{G13}$$

and the momentum density I takes the form

$$I = \alpha u + \alpha^2 u\eta + \frac{1}{3}\alpha\beta u_{xx}, \tag{G14}$$

https://doi.org/10.1017/jfm.2026.11872 Published online by Cambridge University Press

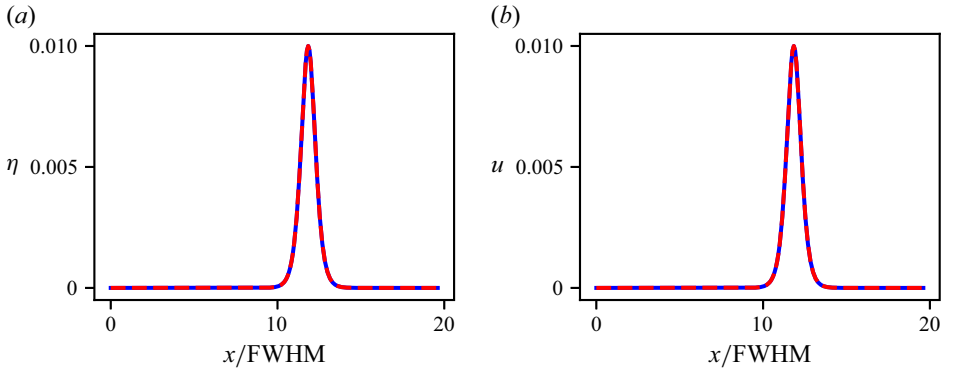


Figure 15. Comparison of the numerical (solid blue) and analytical (dashed red) solutions for (*a*) surface elevation and (*b*) velocity for the full KB system at $t = 2\tau_s$.

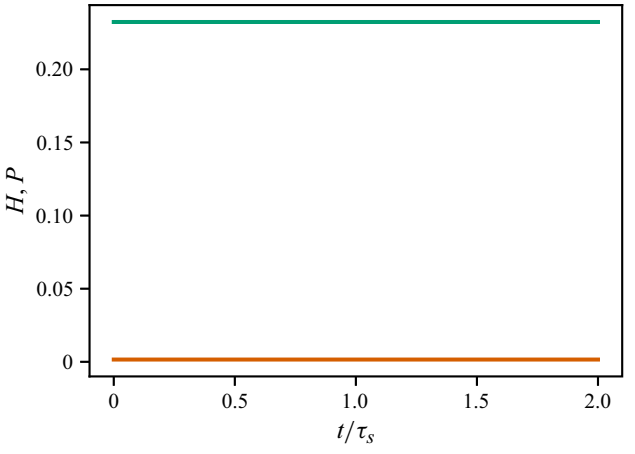


Figure 16. Total momentum P (green line) and energy H (orange line) plotted at each time step over the duration of $2\tau_s$ for the full KB system.

as presented in Ali *et al.* (2017). Figure 16 demonstrates that the energy H and the momentum P remain constant for the duration of the simulation.

G.3. *Validation of the KdV equation*

We begin by considering the linear part of the KdV equation. Setting $\alpha = 0$ in (F1) leaves

$$\eta_t + \eta_x + \frac{1}{6}\beta\eta_{xxx} = 0, \tag{G15}$$

which has an analytical solution of the form $\eta(x, t) = \sin(kx - wt)$ with $\omega = k - (\beta/6)k^3$. For this test case, we set $\beta = 1$ and use (G15) with $t = 0$ as our initial condition. Figure 17 compares the numerical and analytical solutions after $10T_p$. As expected from the integrating factor scheme used, the surface elevation agrees with the analytical result to machine precision. Proceeding with the full KdV equation, we set $\alpha = \beta = 1$ and take a known soliton solution:

$$\eta(x, t) = 2(c - 1)\mathrm{sech}^2\left[\sqrt{\frac{3}{2}(c - 1)}\Big(x - ct\Big)\right] \tag{G16}$$

https://doi.org/10.1017/jfm.2026.11872 Published online by Cambridge University Press

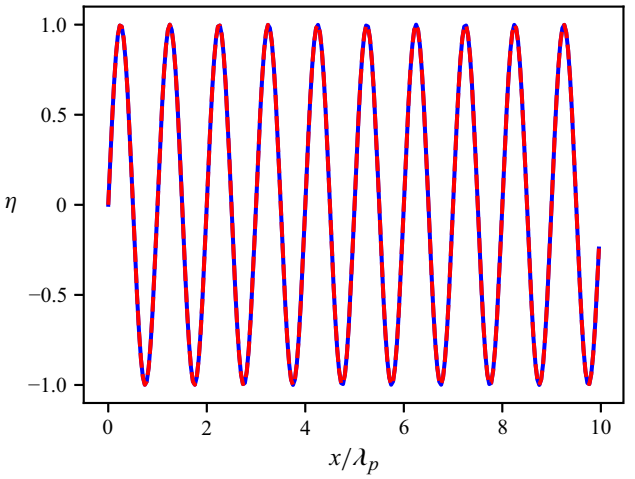


Figure 17. Comparison of the numerical (solid blue) and analytical (red dashed line) solutions for surface elevation for the linear portion of the KdV equation at $t = 10T_p$.

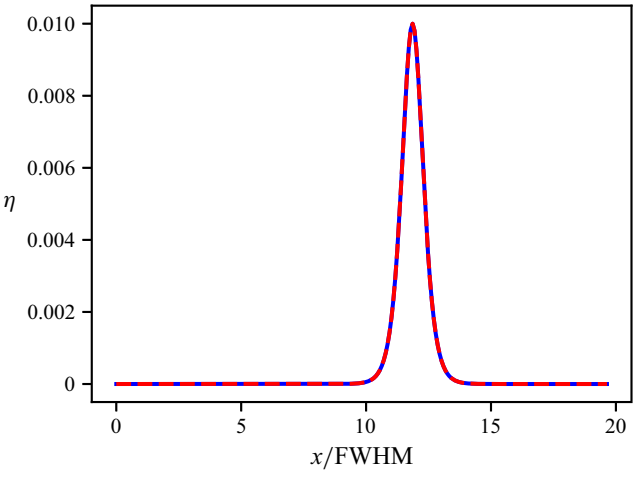


Figure 18. Comparison of the numerical (solid blue) and analytical (dashed red) solutions for surface elevation for the full KdV equation at $t = 2\tau_s$.

with $c = 1.005$ and $t = 0$ for our initial condition. We follow the same procedure as in Appendix G.2 by defining the time scale in terms of τ_s. Figure 18 illustrates the high degree of precision between the numerical and analytical solutions. Conservation of total energy H and total momentum E for KdV is also validated using the integrals defined in (G12); however, in this case, the energy density is defined as

$$E = \alpha^2\eta^2 + \frac{\alpha^3}{4}\eta^3 + \frac{\alpha^2\beta}{6}\eta\eta_{xx} + \frac{\alpha^2\beta}{6}\eta_x^2, \tag{G17}$$

while the momentum density is

$$I = \alpha\eta + \frac{3}{4}\alpha^2\eta^2 + \frac{1}{6}\alpha\beta\eta_{xx}, \tag{G18}$$

https://doi.org/10.1017/jfm.2026.11872 Published online by Cambridge University Press

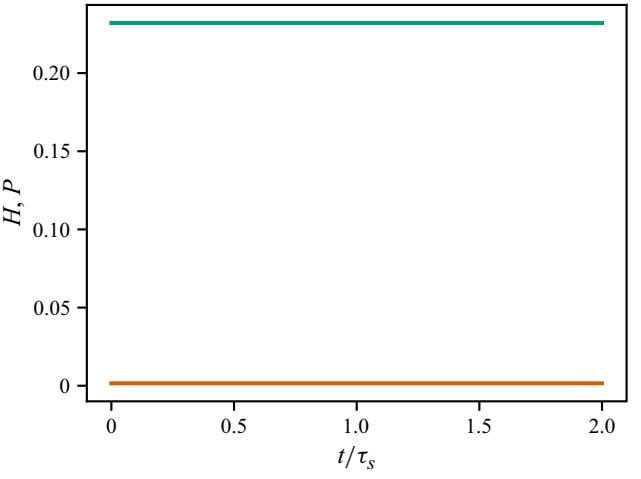


Figure 19. Total momentum P (green line) and energy H (orange line) plotted at each time step over the duration of $2\tau_s$ for the full KdV equation.

as derived in Ali & Kalisch (2013). Figure 19 confirms the conservation of both energy H and momentum P for the duration of the simulation.

Appendix H. Numerical scheme for DST

We solve (3.9) using a finite-difference method on a uniform grid $x_j = -L/2 + j\Delta x$, $j = 0, \ldots, N-1$ and $\Delta x = L/(N-1)$. Defining the grid values by $\Psi_j = \Psi(x_j)$, we approximate $\Psi_{xx}(x_j)$ at the interior points $j = 1, \ldots, N-2$ using a second-order central difference stencil:

$$\frac{\Psi_{j-1} - 2\Psi_j + \Psi_{j+1}}{\Delta x^2} + V_j \Psi_j = 0, \tag{H1}$$

where $V_j := E(\zeta)^2 + ik(\zeta)q(x_j) + r(x_j)$. To capture bound states (elements of the discrete spectrum), we impose asymptotically decaying boundary conditions. That is, for sufficiently large $|x|$

$$\Psi(x) \sim \mathrm{e}^{(-iE|x|)}, \qquad \mathrm{Im}[E] > 0, \tag{H2}$$

so that

$$\Psi_x(x) \sim -iE\,\mathrm{sgn}(x)\Psi(x). \tag{H3}$$

The requirement of $\mathrm{Im}[E] > 0$ places us in the upper half E plane, which ensures decay. These asymptotics lead to Robin boundary conditions:

$$\Psi_x(-L/2) - iE\Psi(-L/2) = 0, \quad \Psi_x(L/2) + iE\Psi(L/2) = 0. \tag{H4}$$

These boundary conditions are applied with second-order one-sided finite differences at the endpoints. At the left boundary we use the forward stencil

$$\frac{-3\Psi_0 + 4\Psi_1 - \Psi_2}{2\Delta x} - iE\Psi_0 = 0, \tag{H5}$$

https://doi.org/10.1017/jfm.2026.11872 Published online by Cambridge University Press

and at the right boundary we use the backward stencil

$$\frac{3\Psi_{N-1} - 4\Psi_{N-2} + \Psi_{N-3}}{2\Delta x} + iE\Psi_{N-1} = 0. \tag{H6}$$

By assembling (H1), (H5), (H6) we obtain an $N \times N$ linear system $A(\zeta)\Psi = 0$. The majority of the matrix $A(\zeta)$ consists of tridiagonal entries corresponding to the interior discretisation, while the boundary conditions are incorporated by modifying the matrix's first and last rows. Bound states correspond to values of ζ for which $A(\zeta)$ is singular, i.e.

$$\det A(\zeta) = 0, \tag{H7}$$

defining a nonlinear eigenvalue problem. Instead of evaluating $\det A(\zeta)$ directly, we locate roots via a Newton iteration of the smallest singular value of $A(\zeta)$ (as zeros of the determinant correspond to points where the smallest singular value is zero). At each iterate ζ, the singular value decomposition $A(\zeta) = U\Sigma V^*$ is computed. From this, we extract the minimal singular value $\sigma := \sigma_{min}(A(\zeta))$ and its corresponding left and right singular vectors u and v, respectively. We can then define the derivative as $\mathrm{d}\sigma/\mathrm{d}\zeta = u^* A'(\zeta) v$, where $A'(\zeta)$ is simply the derivative of the matrix $A(\zeta)$ with respect to ζ (Chen & Dai 2018). The update formula is given by

$$\mathrm{d}\zeta = -\frac{\sigma}{u^* A'(\zeta) v} \tag{H8}$$

so that $\zeta \leftarrow \zeta + \mathrm{d}\zeta$ at each iteration. We iterate until σ falls below some prescribed tolerance, indicating that a root has been located. To ensure robust identification of all roots, we implement a multi-start Newton method by selecting the initial value of ζ from a sufficiently fine mesh spanning the complex ζ plane. We remark that for $\beta > 0$, bound states correspond either to purely imaginary eigenvalues ($\zeta = i\eta$, $\eta \in \mathbb{R}$) or to complex-conjugate pairs ($\zeta_2 = -\zeta_1^*$), as in the case of breathers in the sine-Gordon equation (Kaup 1975).

The criterion for the robustness of bound states corresponding to solitons can be stated in terms of the soliton velocity. The velocity profile for a KB soliton is given by

$$u(x,t) = \frac{2(c_s^2 - 1)}{\alpha \cosh\left(\sqrt{\frac{3}{\beta}(c_s^2 - 1)}(x - c_s t)\right) + c_s}, \tag{H9}$$

where c_s is the soliton velocity, which can be computed via the discrete eigenvalues ζ (Kaup 1975). To ensure physical realisability, the soliton velocity must satisfy $|c_s| > 1$. This condition ensures that the quantity K corresponding to $\sqrt{(3/\beta)(c_s^2 - 1)}$ appearing in the hyperbolic cosine argument of (H9) remains real and positive. The parameter K controls the inverse width of the soliton profile, i.e. width $\propto 1/K$; therefore, solitons with velocities closer to 1 (corresponding to eigenvalues closer to the continuous spectrum) exhibit broad profiles with slow decay in the physical domain. These solitons may not be realisable in a finite domain due to their excessive width. Solitons with larger velocities correspond to narrower, more strongly localised solitons. This is consistent with the definition of 'true' bound states where the tails decay to zero as $|x| \to \infty$. In the ζ plane, the continuous spectrum corresponds to $\mathrm{Im}[E(\zeta)] = 0$, i.e. $\zeta \in \mathbb{R}$ or $|\zeta| = \sqrt{3/\beta}$. We therefore retain only discrete eigenvalues satisfying $|c_s| > 1$ and separated from the continuous spectrum curve by at least a 1 % buffer, $\left||\zeta| - \sqrt{3/\beta}\right| > 0.01\sqrt{3/\beta}$. Any discrete eigenvalue that does not satisfy this condition is deemed spurious and is not included in the computation of the soliton energy presented in § 3.2.1.

https://doi.org/10.1017/jfm.2026.11872 Published online by Cambridge University Press

References

Agafontsev, D.S. & Zakharov, V.E. 2015 Integrable turbulence and formation of rogue waves. *Nonlinearity* **28** (8), 2791.

Agafontsev, D.S. & Zakharov, V.E. 2016 Integrable turbulence generated from modulational instability of cnoidal waves. *Nonlinearity* **29** (11), 3551.

Ali, A., Juliussen, B.-S. & Kalisch, H. 2017 Approximate conservation laws for an integrable boussinesq system. *Math. Model. Nat. Phenom.* **12** (1), 1–14.

Ali, A. & Kalisch, H. 2013 On the formulation of mass, momentum and energy conservation in the KdV equation. *Acta Appl. Math.* **133** (1), 113–131.

Annenkov, S.Y. & Shrira, V.I. 2006 Role of non-resonant interactions in the evolution of nonlinear random water wave fields. *J. Fluid Mech.* **561**, 181–207.

Banks, J.W., Buckmaster, T., Korotkevich, A.O., Kovačič, G. & Shatah, J. 2022 Direct verification of the kinetic description of wave turbulence for finite-size systems dominated by interactions among groups of six waves. *Phys. Rev. Lett.* **129**, 034101.

Bhrawy, A.H., Tharwat, M.M. & Abdelkawy, M.A. 2013 Integrable system modelling shallow water waves: Kaup–Boussinesq shallow water system. *Indian J. Phys.* **87** (7), 665–671.

Bona, J.L., Chen, M. & Saut, J.-C. 2002 Boussinesq equations and other systems for small-amplitude long waves in nonlinear dispersive media. I: derivation and linear theory. *J. Nonlinear Sci.* **12** (4), 283–318.

Bona, J.L., Chen, M. & Saut, J.-C. 2004 Boussinesq equations and other systems for small-amplitude long waves in nonlinear dispersive media: II. The nonlinear theory. *Nonlinearity* **17** (3), 925.

Bonnemain, T., Doyon, B. & El, G. 2022 Generalized hydrodynamics of the KdV soliton gas. *J. Phys. A: Math. Theor.* **55** (37), 374004.

Chen, X.-P. & Dai, H. 2018 A modified newton method for nonlinear eigenvalue problems. *East Asian J. Appl. Maths* **8** (1), 139–150.

Colléaux, C., Skipp, J., Nazarenko, S. & Laurie, J. 2025 A bound state attractor in optical turbulence. *Phys. D: Nonlinear Phenom.* **477**, 134687.

Dyachenko, A.I., Korotkevich, A.O. & Zakharov, V.E. 2003 Decay of the monochromatic capillary wave. *J. Expl Theor. Phys. Lett.* **77** (9), 477–481.

Dyachenko, A.I., Korotkevich, A.O. & Zakharov, V.E. 2004 Weak turbulent Kolmogorov spectrum for surface gravity waves. *Phys. Rev. Lett.* **92**, 134501.

El, G.A. 2021 Soliton gas in integrable dispersive hydrodynamics. *J. Stat. Mech.: Theory Exp.* **2021** (11), 114001.

El, G.A., Grimshaw, R.H.J. & Pavlov, M.V. 2001 Integrable shallow-water equations and undular bores. *Stud. Appl. Maths* **106** (2), 157–186.

Flamarion, M.V. & Pelinovsky, E. 2024 Nonlinear random wave fields within a Boussinesq system. *Phys. Lett. A* **520**, 129677.

Gong, R. & Wang, D.-S. 2022 Formation of the undular bores in shallow water generalized Kaup–Boussinesq model. *Phys. D: Nonlinear Phenom.* **439**, 133398.

Hasselmann, K. 1962 On the non-linear energy transfer in a gravity-wave spectrum Part 1. General theory. *J. Fluid Mech.* **12** (4), 481–500.

Hrabski, A. & Pan, Y. 2020 Effect of discrete resonant manifold structure on discrete wave turbulence. *Phys. Rev. E* **102** (4), 041101.

Hrabski, A. & Pan, Y. 2024 Verification of wave turbulence theory in the kinetic limit. *Phys. Rev. Res.* **6**, 023184.

Ivanov, R. 2009 Two-component integrable systems modelling shallow water waves: the constant vorticity case. *Wave Motion* **46** (6), 389–396.

Janssen, P.A.E.M. 2003 Nonlinear four-wave interactions and freak waves. *J. Phys. Oceanogr.* **33** (4), 863–884.

Juliussen, B.-S.H. 2014 Investigations of the Kaup–Boussinesq model equations for water waves. Master thesis, The University of Bergen, Norway.

Kaihatu, J.M., Veeramony, J., Edwards, K.L. & Kirby, J.T. 2007 Asymptotic behavior of frequency and wave number spectra of nearshore shoaling and breaking waves. *J. Geophys. Res.: Oceans* **112** (C6).

Karczewska, A. & Rozmej, P. 2018 *Shallow Water Waves: Extended Korteweg-de Vries Equations: Second Order Perturbation Approach*. Oficyna Wydawnicza Uniwersytetu Zielonogórskiego.

Kaup, D.J. 1975 A higher-order water-wave equation and the method for solving it. *Prog. Theor. Phys.* **54** (2), 396–408.

Klein, C. & Saut, J.-C. 2025 On the Kaup–Broer–Kupershmidt systems. *EMS Surv. Math. Sci.* **12** (1), 215–242.

https://doi.org/10.1017/jfm.2026.11872 Published online by Cambridge University Press

KOROTKEVICH, A.O. 2023 Inverse cascade spectrum of gravity waves in the presence of a condensate: a direct numerical simulation. *Phys. Rev. Lett.* **130**, 264002.

KOROTKEVICH, A.O., DYACHENKO, A.I. & ZAKHAROV, V.E. 2016 Numerical simulation of surface waves instability on a homogeneous grid. *Phys. D: Nonlinear Phenom.* **321–322**, 51–66.

KRASITSKII, V.P. 1994 On reduced equations in the Hamiltonian theory of weakly nonlinear surface waves. *J. Fluid Mech.* **272**, 1–20.

KUPERSHMIDT, B.A. 1985 Mathematics of dispersive water waves. *Commun. Math. Phys.* **99** (1), 51–73.

LEDUQUE, T., KACZMAREK, M., MICHALLET, H., BARTHÉLEMY, E. & MORDANT, N. 2025 From deep to shallow water two-dimensional wave turbulence: emergence of soliton gas. *Phys. Rev. Fluids* **10**, 114801.

CLARK DI LEONI, P., COBELLI, P.J. & MININNI, P.D. 2014 Wave turbulence in shallow water models. *Phys. Rev. E* **89**, 063025.

L'VOV, V.S. & NAZARENKO, S. 2010 Discrete and mesoscopic regimes of finite-size wave turbulence. *Phys. Rev. E* **82** (5), 056322.

NAZARENKO, S. 2011 *Wave Turbulence*. Springer.

ONORATO, M., OSBORNE, A.R., JANSSEN, P.A.E.M. & RESIO, D. 2009 Four-wave resonant interactions in the classical quadratic Boussinesq equations. *J. Fluid Mech.* **618**, 263–277.

PAN, Y. 2020 High-order spectral method for the simulation of capillary waves with complete order consistency. *J. Comput. Phys.* **408**, 109299.

PAN, Y. & YUE, D.K.P. 2017 Understanding discrete capillary-wave turbulence using a quasi-resonant kinetic equation. *J. Fluid Mech.* **816**, R1.

PELINOVSKY, E. & SERGEEVA (KOKORINA), A. 2006 Numerical modeling of the KdV random wave field. *Eur. J. Mech. - B/Fluids* **25** (4), 425–434.

RANDOUX, S., WALCZAK, P., ONORATO, M. & SURET, P. 2016 Nonlinear random optical waves: integrable turbulence, rogue waves and intermittency. *Phys. D: Nonlinear Phenom.* **333**, 323–335.

REDOR, I., BARTHÉLEMY, E., MICHALLET, H., ONORATO, M. & MORDANT, N. 2019 Experimental evidence of a hydrodynamic soliton gas. *Phys. Rev. Lett.* **122**, 214502.

REDOR, I., MICHALLET, H., MORDANT, N. & BARTHÉLEMY, E. 2021 Experimental study of integrable turbulence in shallow water. *Phys. Rev. Fluids* **6** (12), 124801.

ROBERTI, G., EL, G., RANDOUX, S. & SURET, P. 2019 Early stage of integrable turbulence in the one-dimensional nonlinear Schrödinger equation: a semiclassical approach to statistics. *Phys. Rev. E* **100**, 032212.

SURET, P., RANDOUX, S., GELASH, A., AGAFONTSEV, D., DOYON, B. & EL, G. 2024 Soliton gas: theory, numerics, and experiments. *Phys. Rev. E* **109**, 061001.

TREFETHEN, L.N. 2000 Spectral methods in MATLAB. *Soc. Ind. Appl. Maths* **10**, 101–114.

WU, B., ONORATO, M., HANI, Z. & PAN, Y. 2025 Validity condition of normal form transformation for the β-FPUT system, arXiv: 2510.04831.

ZAKHAROV, V.E. 1991 *What Is Integrability? Springer Series in Nonlinear Dynamics*. Springer.

ZAKHAROV, V. 1999 Statistical theory of gravity and capillary waves on the surface of a finite-depth fluid. *Eur. J. Mech. - B/Fluids* **18** (3), 327–344. Three-Dimensional Aspects of Air-Sea Interaction.

ZAKHAROV, V.E. & SCHULMAN, E.I. 1980 Degenerative dispersion laws, motion invariants and kinetic equations. *Phys. D: Nonlinear Phenom.* **1** (2), 192–202.

ZAKHAROV, V.E. & SCHULMAN, E.I. 1988 On additional motion invariants of classical Hamiltonian wave systems. *Phys. D: Nonlinear Phenom.* **29** (3), 283–320.

ZAKHAROV, V.E., L'VOV, V.S. & FALKOVICH, G. 2012 *Kolmogorov Spectra of Turbulence I: Wave Turbulence*. Springer Science & Business Media.

ZHANG, Z. & PAN, Y. 2022*a* Forward and inverse cascades by exact resonances in surface gravity waves. *Phys. Rev. E* **106** (4), 044213.

ZHANG, Z. & PAN, Y. 2022*b* Numerical investigation of turbulence of surface gravity waves. *J. Fluid Mech.* **933**, A58.

https://doi.org/10.1017/jfm.2026.11872 Published online by Cambridge University Press